Computational Investigation of Copper Phosphides as Conversion Anodes for Lithium-Ion Batteries

Angela F. Harper,*,† Matthew L. Evans,*,† and Andrew J. Morris*,‡

†*Theory of Condensed Matter, Cavendish Laboratory, University of Cambridge, J. J. Thomson Avenue, Cambridge CB3 0HE, U.K.*

‡*School of Metallurgy and Materials, University of Birmingham, Edgbaston, Birmingham B15 2TT, U.K*

E-mail: afh41@cam.ac.uk; me388@cam.ac.uk; a.j.morris.1@bham.ac.uk

Abstract

Using first principles structure searching with density-functional theory (DFT) we identify a novel $Fm\bar{3}m$ phase of Cu_2P and two low-lying metastable structures, an $I\bar{4}3d$–Cu_3P phase, and a Cm–Cu_3P_{11} phase. The computed pair distribution function of the novel Cm–Cu_3P_{11} phase shows its structural similarity to the experimentally identified Cm–Cu_2P_7 phase. The relative stability of all Cu–P phases at finite temperatures is determined by calculating the Gibbs free energy using vibrational effects from phonon modes at 0 K. From this, a finite-temperature convex hull is created, on which $Fm\bar{3}m$–Cu_2P is dynamically stable and the $Cu_{3-x}P$ ($x < 1$) defect phase $Cmc2_1$–Cu_8P_3 remains metastable (within 20 meV/atom of the convex hull) across a temperature range from 0 K to 600 K. Both CuP_2 and Cu_3P exhibit theoretical gravimetric capacities higher than contemporary graphite anodes for Li-ion batteries; the predicted Cu_2P phase has a theoretical gravimetric capacity of 508 mAh/g as a Li-ion

battery electrode, greater than both Cu_3P (363 mAh/g) and graphite (372 mAh/g). Cu_2P is also predicted to be both non-magnetic and metallic, which should promote efficient electron transfer in the anode. Cu_2P's favorable properties as a metallic, high-capacity material suggest its use as a future conversion anode for Li-ion batteries; with a volume expansion of 99 % during complete cycling, Cu_2P anodes could be more durable than other conversion anodes in the Cu–P system with volume expansions greater than 150 %. The structures and figures presented in this paper, and the code used to generate them, can be interactively explored online using Binder.

Introduction

Graphite is the most commonly employed lithium-ion battery (LIB) anode, but is inherently limited by a maximum theoretical capacity of 372 mAh/g upon formation of LiC_6. Phosphorus (black or red) has a significantly higher theoretical capacity of 2596 mAh/g due to the formation of Li_3P; however it suffers from capacity deterioration, primarily caused by deleterious volume expansion that occurs upon charging, which constrains the capacity to 350–500 mAh/g in a limited voltage window.[1] In addition, P and its lithiated phases have limited electrical conductivity, requiring dopants and additives to improve performance. By adding transition metals to P, through nanostructuring or synthesis, both electrical conductivity and stability during cycling can be enhanced.[2]

Transition metal phosphides (TMP) provide a large design space in which to engineer such high-capacity, conversion anodes for LIBs.[3] High-throughput computational screening has previously identified TMPs with high capacities for LIB electrodes including TiP, Co_2P, Mn_2P and others.[4] As conversion anodes for LIBs, TMPs offer both added gravimetric capacity (ranging from 500 to 2000 mAh/g[4]) and stability against volume expansion over several battery cycles.[5] In addition to bulk or powdered TMPs being used as LIB conversion anodes,[6] nanostructured TMPs can often display improved electrochemical cycling performance.[7] Despite these efforts, TMPs have yet to be widely adopted as conversion anodes,

given the large volume expansion (between 150 % to 300 %[4]) exhibited by anodes with high P content, which limits their cyclability. Despite this drawback in volume expansion, TMPs show higher average voltages than graphite, which has an average voltage of 0.1 V. For example, CoP has an average voltage of 0.67 V, the ternary metal phosphide LiFeP has an average voltage of 0.4 V, and MnP has an average voltage of 0.62 V.[4] Higher average voltages give the metal phosphides improved safety while sacrificing energy density, making them an ideal choice for large-scale and long-term energy storage.

Several previously studied TMP anodes include $FeP_{x=1,2,4}$,[8] Fe_2P nanoparticles,[9] Ni_2P,[10] CuP_2,[11,12] and Cu_3P,[13,14] among others. Of the TMPs tested as conversion anodes, the copper phosphides (specifically CuP_2 and Cu_3P) have shown promise for their cyclability and capacity. The copper phosphides offer additional benefits to the other TMPs, as Cu is already used as a common current collector, providing further cycling capability and resistance to degradation.[15] Cu_3P prepared by high temperature synthesis had a first-cycle capacity of 527 mAh/g,[13] and a porous Cu_3P anode synthesized by facile chemical corrosion exhibited a capacity between 360–380 mAh/g over 70 cycles.[16] The capacity of high temperature synthesized Cu_3P exceeds that of graphite, and the cyclability of porous Cu_3P is improved relative to other Cu_3P anodes.[13,17] CuP_2 on the other hand, delivers a higher initial capacity of 815 mAh/g, but can only be cycled stably 10 times before the capacity fades to 360 mAh/g.[12] The main factor in this degradation is the high concentration of P in the CuP_2 which, while enabling high capacity, also contributes to the structural instability of CuP_2 during cycling as the lithium-rich Li_3P phase forms. To optimize the trade-off between stability and capacity, it would be beneficial to discover a compound with higher P content than Cu_3P to offer higher capacity, and with a Cu content higher than CuP_2 to aid in cyclability.

By performing crystal structure prediction, combining both *ab initio* random structure searching (AIRSS) and a genetic algorithm (GA), in addition to structural prototyping with known crystal structures of related chemistries,[18–20] we produced the compositional phase diagram of the copper phosphide system. We describe this approach to structure prediction

and the application of open source Python packages `matador` (v0.9),[21] for high-throughput first principles calculations, and `ilustrado` (v0.3),[22] for computational structure prediction with GAs. Crystal structure prediction for battery anodes is a well-tested method,[23] used for identifying both novel anode materials,[4] and unknown phases which form during battery cycling.[24,25] AIRSS has been used previously to search for additional phases of Li–P and Na–P which form during battery cycling.[26] The GA was also employed to search for new phases of Na–P, which were confirmed experimentally through solid-state nuclear magnetic resonance (NMR) spectroscopy.[27] As applied here to Cu–P, these methods predict a novel metallic $Fm\bar{3}m$–Cu_2P phase at 0 K, within the target composition range of $Cu_{1<x<3}P$, for a high-capacity, low volume expansion conversion anode; we compare its electronic structure to other TMPs to show a similarity to $Fm\bar{3}m$-Rh_2P and $Fm\bar{3}m$-Ir_2P. Two other phases, Cm–Cu_3P_{11} and $I\bar{4}3d$–Cu_3P are identified as metastable, both bearing structural similarity to known copper phosphides. We calculate the convex hull of Cu–P at temperatures up to 600 K, confirming the dynamic and chemical stability of Cu_2P across this temperature range. A ground-state voltage profile from density-functional theory (DFT), shows that $Fm\bar{3}m$–Cu_2P undergoes the same lithiation process as $P6_3cm$–Cu_3P; however $Fm\bar{3}m$–Cu_2P has a higher capacity of 508 mAh/g, with an average voltage of 0.86 V versus Li/Li^+ (compared to 0.91 V for $P6_3cm$–Cu_3P).

Methods

To search for novel copper phosphides, we first performed structural relaxations of the 13 structures from the Inorganic Crystal Structure Database (ICSD)[28] of Cu_xP ($0 < x < 1$). The Python package `matador`[21] was used to query 1053 prototype binary structures from the Open Quantum Materials Database (OQMD)[19] with chemical compositions containing a pnictogen and a transition metal from the first two rows, namely {Ti, V, Cr, Mn, Fe, Co, Ni, Cu, Zn, Zr, Nb, Mo, Tc, Ru, Rh, Pd, Ag, Cd}–{P, As, Sb}; each composition was

then transmuted to the corresponding stoichiometry of Cu–P, yielding 909 unique structures after geometry optimization. In order to extend this search beyond existing prototypes, two additional structure prediction steps were performed, namely AIRSS[29] and an evolutionary search with the GA implemented in the `ilustrado`[22] package.

When performing AIRSS, one proceeds by generating random "sensible" (symmetry, density and atomic separation constrained) trial cells and then geometry optimizing them to their corresponding local minima. All relaxations can be performed concurrently, with no interdependence between calculations. New trial structures are generated until the ground state of each stoichiometry (within the constraints of the search) has been found multiple times.

We initially performed an exploratory AIRSS search consisting of around 5000 trial structures, with constraints on cell size, stoichiometry, and number of atoms in the cell. In this initial search, the total number of atoms in the cell was constrained to be ≤ 40, and the total number of formula units was randomized between 1 and 4, while still keeping the total number of atoms below 40. The number of atoms of Cu and P were randomized between 1 and 9 in each cell, and the cell volume (V) was constrained based on the total number of atoms in the cell (N) to be $8N\,\text{Å}^3 \leq V \leq 20N\,\text{Å}^3$, based on the average densities of Cu–P phases within the ICSD.

Structures from the searching and enumeration procedures were then used, with fitness weighted according to their distance from the convex hull, as the initial configurations for a GA implemented in the Python package `ilustrado`.[22] The `ilustrado` package uses a simple cut-and-splice crossover operation, supplemented by mutation operators (random noise, atomic permutations, vacancies and adatoms).[30] To avoid stagnation, each trial structure was filtered for similarity (via pair distribution function overlap) against existing structures in the population. Three independent GA runs were performed with 10 generations each, yielding a further 1049 relaxed structures. Finally, a directed AIRSS search of Cu_xP_y where $x+y < 8$, was performed to create a final set of ~20,000 structures within the Cu–P chemical

space. In all cases, to constrain the search to physically reasonable structures, a minimum atomic separation of 1.5 Å was enforced and the maximum number of atoms in the cell was constrained to 10 for the initial ~10,000 AIRSS searches and 40 atoms per cell for the final ~3,000 trials.

All calculations were performed using CASTEP (v18.1 and v19.1), the plane wave pseudopotential DFT package.[31] To maximize computational efficiency, the initial calculations were performed with loose convergence criteria that ensured formation energies converged to 10 meV/atom. The Perdew-Burke-Ernzerhof (PBE) exchange-correlation functional was used[32] with Vanderbilt ultrasoft pseudopotentials[33] that required a plane wave kinetic energy cutoff of 300 eV to converge energies to within 10 meV/atom. The Brillouin zone (BZ) was sampled with a Monkhorst-Pack grid k-point spacing finer than $2\pi \times 0.05$ Å^{-1}; the grid was frequently recomputed to accommodate any changes in cell shape and size during relaxation. Each structure was geometry optimized at this accuracy to a force tolerance of 0.05 eV/Å. The structures with a formation energy within 50 meV of the convex hull were then further optimized once more using CASTEP's on-the-fly (OTF) "C18" library of ultrasoft pseudopotentials[1] with a finer k-point sampling of $2\pi \times 0.03$ Å^{-1} and plane wave kinetic energy cutoff of 500 eV, which yielded formation energies converged to within 2.5 meV/atom. In order to predict the voltage profiles with the same convergence criteria (formation energies within 2.5 meV/atom), the relaxation of known Li–P structures required a higher plane wave cutoff of 700 eV. Therefore, to compare ternary phases of Cu–Li–P in the voltage profile, all Cu–Li–P phases were re-optimized at a plane wave kinetic energy cutoff of 700 eV.

To identify stable structures from this search, a convex hull of the copper phosphides was created. The formation energy E_f of each structure Cu_xP_y was calculated using,

$$E_f(Cu_xP_y) = E(Cu_xP_y) - xE(Cu) - yE(P), \quad (1)$$

[1]OTF pseduopotential strings are Cu: 3|2.2|2.0|1.0|10|12|13|40:41:32(qc=6), P: 3|1.8|4|4|5|30:31:32, Li: 1|1.0|14|16|18|10U:20(qc=7)

where E(Cu) is the DFT total energy of the $Fm\bar{3}m$–Cu structure, and E(P) is the energy of $Cmca$-P (black phosphorus). Black phosphorus was used as the P chemical potential instead of the lower energy polymorph red phosphorus; as has been previously discussed in Mayo *et al.*,[26] black phosphorus is commonly used when making electrochemical cells.[34]

Electrochemical voltage profiles for Li insertion into the stable Cu–P phases were calculated from the computed formation energies from ternary convex hull of Cu–Li–P. In order to calculate the voltage profiles shown in the section on Cu_2P as a Li-ion battery conversion anode, the voltage, $\bar{V}$, between two tie-lines in the ternary convex hull with compositions $Li_{x_1}Cu_nP$ and $Li_{x_2}Cu_nP$ was calculated using,

$$\bar{V}(x_1, x_2) = -\frac{E(\mathrm{Li}_{x_1}\mathrm{Cu}_n\mathrm{P}) - E(\mathrm{Li}_{x_2}\mathrm{Cu}_n\mathrm{P}) - (x_1 - x_2)E(\mathrm{Li})}{(x_1 - x_2)F}, \tag{2}$$

as stated by Urban et al.[35] In equation 2, $E(Li_{x_1}Cu_nP)$ and $E(Li_{x_2}Cu_nP)$ are the ground state energies of two phases on along the reaction pathway of the ternary convex hull, in which x_1 and x_2 are the relative amounts of Li in the starting and ending products at each point in the pathway.

All phonon calculations were performed under the harmonic approximation with the PBE xc-functional in a $2 \times 2 \times 2$ supercell (corresponding to a phonon q-point spacing of $2\pi \times 0.046\,\text{Å}^{-1}$ for $Fm\bar{3}m$-Cu_2P) using the finite displacement method implemented in the CASTEP code. The dynamical matrix was then Fourier interpolated onto the BZ path provided by the SeeK-path Python package[36,37] to compute the phonon dispersion, and onto a fine Monkhorst-Pack grid to compute the phonon density of states.

The band structure for Cu_2P was calculated using the higher accuracy parameters and pseudopotentials mentioned previously, and the electronic density of states was integrated and projected onto atomic orbitals using the OptaDOS code.[38,39] Vibrational properties of all stable phases were computed using the finite displacement method, with an added many-body dispersion correction (MBD denoted MBD* in CASTEP v19.0)[40] to account for inter-layer interactions in black phosphorus.

The open source Python package `matador` (v0.9)[21] was used to run the CASTEP calculations, perform the analysis and create the plots found in this article. All of this analysis, as well as the underlying source code and data, can be explored interactively using Binder and found on Github `harpaf13/data.copper-phosphides`. The input and output files associated with our calculations have been deposited into the Cambridge Repository at https://doi.org/10.17863/CAM.52272.

Results

From the search of ~20,000 trial structures, there are 42 unique phases within 50 meV/atom of the convex hull. Previous computational structure searches have used a distance above the hull of 25 meV/atom,[41] and given the accuracy of PBE,[42] we chose to increase this cutoff to 50 meV/atom. Furthermore the experimentally verified $P6_3cm$–Cu_3P structure[43] is 37 meV/atom above the convex hull tie-line, further justifying this cut-off. Uniqueness was determined by computing pairwise overlap integrals of the pair distribution functions of phases at each stoichiometry using `matador`. The set of 42 unique phases contains four experimentally reported copper phosphides from the ICSD; $P\bar{1}$–CuP_{10} synthesized by a mineralization reaction,[44] $C2/m$–Cu_2P_7,[45] $P2_1/c$–CuP_2[45] and $P6_3cm$–Cu_3P[43,46] from high temperature sintering.

Oloffson's experiments on single crystal $P6_3cm$–Cu_3P synthesized at high temperature, and subsequent work by deTrizio et al.,[47] show that Cu_3P has several defects[43] with a range of stoichiometries between $Cu_{2.6}P$ and $Cu_{2.8}P$. DFT studies of the Cu vacancies indicate that Cu_3P is substoichiometric[47] and to search this substoichiometric space, unit cells of $P6_3cm$–$Cu_{18}P_6$ were enumerated with 1, 2, and 3 Cu vacancies, resulting in 76 $Cu_{3-x}P$ structures. The lowest energy defect was a $Cmc2_1$–Cu_8P_3 ($Cu_{2.67}P$) phase 26 meV/atom above the convex hull tie-line, denoted as Vacancy enumeration in Figure 1.

The convex hull of Cu–P, with points colored by the provenance of each structure, is

presented in Figure 1; the experimentally identified phases, and a new $Fm\bar{3}m$–Cu_2P phase, all lie on the convex hull tie-line and are each labeled with an arrow.

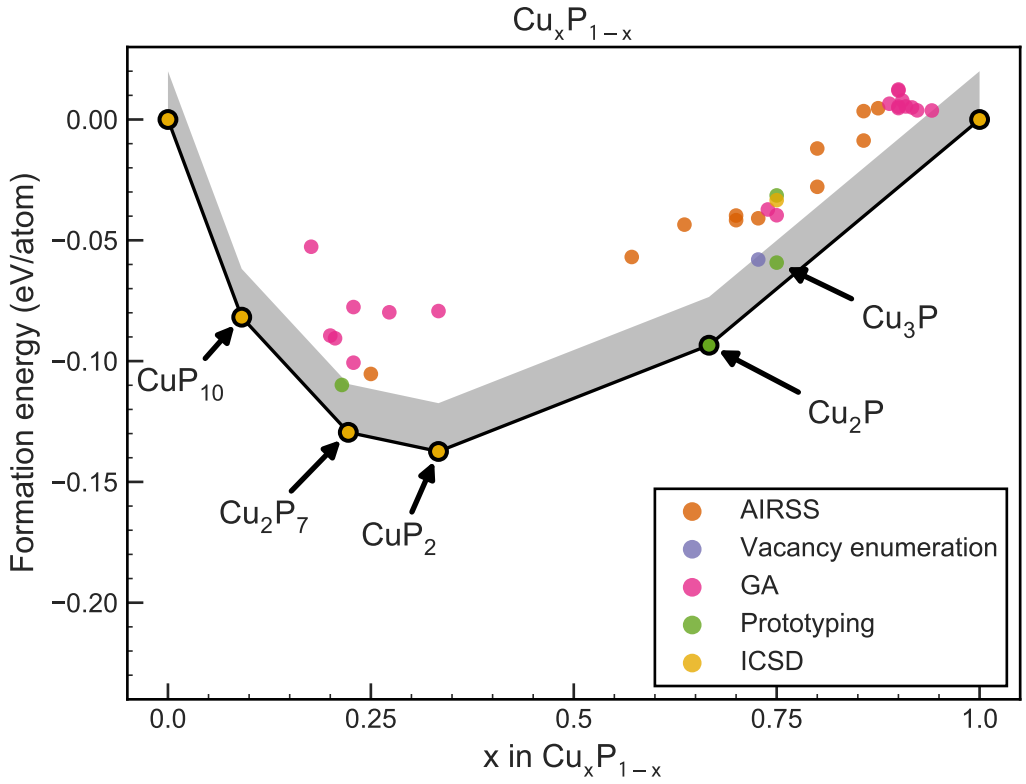

Figure 1: Convex hull of Cu–P phases from structure searching. Four structures lie on the convex hull, CuP_{10}, Cu_2P_7, CuP_2, and Cu_2P. Structures are colored according to their provenance: either from a searching method (AIRSS, GA, Prototyping, Vacancy enumeration) or from an existing database (ICSD). Prototyping refers to using a prototype structure from the ICSD, and replacing the atoms with Cu or P as described in the Methods section. The Vacancy Enumeration phases are the phases optimized after adding Cu vacancies to $P6_3cm$–Cu_3P. Phases within 20 meV/atom of the convex hull lie within the shaded gray region, and Cu_3P is labeled for reference.

Details of the 24 structures which are both negative in formation energy relative to Cu and P, and are within 50 meV/atom of the convex hull are given in Table 1. Phases on the convex hull tie-line in Figure 1 are indicated with $\star$ in Table 1 and phases which are experimentally confirmed are highlighted in light gray. Phases not reported previously, within 20 meV/atom of the convex hull tie-line, are highlighted in dark gray in Table 1. The provenance of each phase is given in the last column of Table 1. Phases from the ICSD are denoted with their

Table 1: Phases of Cu–P with formation energy ≤ 0 meV/atom relative to Cu and P, and the distance from the convex hull tie-line, ΔE, less than 50 meV/atom.

Formula	On Tie-line	ΔE (meV/atom)	Spacegroup	Provenance
Cu	⋆	-	$Fm\bar{3}m$	ICSD 43493[a]
Cu_6P		31	$I4/mmm$	AIRSS
Cu_4P		28	$P4/nmm$	AIRSS
Cu_4P		44	$Cmmm$	AIRSS
Cu_3P		11	$I\bar{4}3d$	Prototype 64715[b]
Cu_3P		30	$P2_1/m$	GA
Cu_3P		37	$P6_3cm$	ICSD 15056[c]
Cu_3P		39	$I\bar{4}$	Prototype 23560[d]
$Cu_{17}P_6$		40	$P1$	GA
Cu_8P_3		26	$Cmc2_1$	AIRSS
Cu_8P_3		36	$P6_3cm$	AIRSS
Cu_8P_3		39	$P1$	AIRSS
Cu_7P_3		42	$P1$	AIRSS
Cu_7P_3		44	$P1$	AIRSS
Cu_2P	⋆	-	$Fm\bar{3}m$	Prototype 38356[e]
Cu_4P_3		49	$P4/nmm$	AIRSS
CuP_2	⋆	-	$P2_1/c$	ICSD 35282[f]
CuP_3		26	$Pmmn$	AIRSS
Cu_8P_{27}		29	Cm	GA
Cu_8P_{27}		43	Cm	GA
Cu_2P_7	⋆	-	$C2/m$	ICSD 35281[g]
Cu_3P_{11}		17	Cm	Prototype 26563[h]
Cu_7P_{27}		33	Cm	GA
CuP_4		32	Cm	GA
CuP_{10}	⋆	-	$P\bar{1}$	ICSD 418805[i]
P	⋆	-	$Cmca$	ICSD 150873[j]

Light gray indicates experimentally confirmed phases
Dark gray indicates new phases with $\Delta E \leq 20$ meV/atom
[a]Experimental lattice parameter for Cu from [48]
[b]Prototype structure is $I\bar{4}3d$–Cu_3As [49]
[c]Structure from single crystal diffractometry [43]
[d]Prototype structure $I\bar{4}$–Cr_3P by single crystal X-ray diffraction [50]
[e]Prototype structure $Fm\bar{3}m$–Rh_2P by X-ray diffraction [51]
[f]Structure from X-ray diffraction [45]
[g]Structure from X-ray diffraction [45]
[h]Prototype structure Cm–Ag_3P_{11} by single crystal X-ray diffraction [52]
[i]Structure from single crystal X-ray diffraction [44]
[j]Black phosphorus structure from powder X-ray diffraction [53]

ICSD Collection Code as "ICSD #" . Phases which were found by swapping the elements of a prototype ICSD structure are denoted by the ICSD structure of the prototype used as "Prototype #".

Of the 24 binary structures in Table 1, 9 were discovered by AIRSS, 6 by the GA, 4 from structural prototyping, and 4 were previously known Cu–P structures from the ICSD. Of particular interest are three new phases, highlighted in dark gray in Table 1, $Fm\bar{3}m$–Cu_2P, $I\bar{4}3d$–Cu_3P and Cm–Cu_3P_{11} which are all within 20 meV/atom of the convex hull and will be discussed further in the following sections.

Phosphorus rich phase Cm–Cu_3P_{11}

Cm–Cu_3P_{11} is a new structure which was found by relaxing the prototype Ag_3P_{11} (ICSD 26563); it is 17 meV/atom from the hull tie-line, and has structural similarity to the ICSD structure $C2/m$–Cu_2P_7 (ICSD 35281)[45] as shown in Figure 2. Both of these structures have repeating chains of P atoms, as seen in the supercells in Figure 2, in which alternating patterns of Cu or Cu–P are connected to a zig-zag chain of P atoms. All known phases in the P-rich (Cu_xP where $x < 1$) region of the convex hull, namely $C2/m$–Cu_2P_7 (ICSD 35281),[45] $P2_1/c$–CuP_2 (ICSD 35281),[45] and $P\bar{1}$–CuP_{10} (ICSD 418805),[44] have long chains of P atoms, similar to the layered P_12/c_1-P (ICSD 29273,[54] red P).

In the P-rich region, 5 new phases were identified within 50 meV/atom of the convex hull: $Pmmn$–CuP_3, Cm–Cu_8P_{27}, Cm–Cu_3P_{11}, Cm–Cu_7P_{27} and Cm–CuP_4. Using the GA it was possible to include structures with stoichiometries of P up to 27 atoms in the unit cell, and thus found structural variations on Cu_2P_7 such as Cu_3P_{11}. To compare the new metastable Cm–Cu_3P_{11} structure with other P-rich structures, the pair distribution functions (PDF) and calculated powder x-ray diffraction (PXRD) peaks of CuP_2, Cu_2P_7 and Cu_3P_{11} were calculated and are compared in Figure 3. In all three cases, the initial sharp peak in the PDF between 2.20 and 2.24 Å shows, unsurprisingly, the same Cu–P and P–P distance shared by all three structures. The peaks at radii above 3 Å show the longer range similarity between

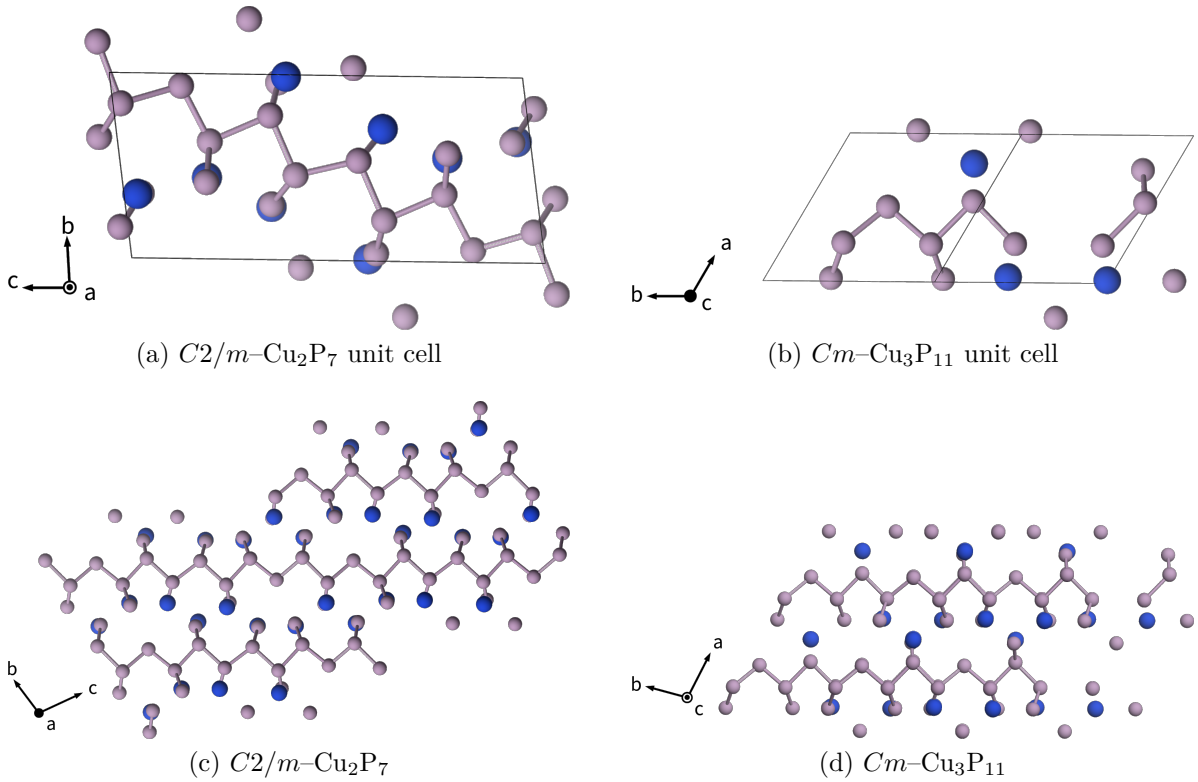

(a) $C2/m$–Cu_2P_7 unit cell

(b) Cm–Cu_3P_{11} unit cell

(c) $C2/m$–Cu_2P_7

(d) Cm–Cu_3P_{11}

Figure 2: (a) Cu_2P_7 unit cell (b) Cu_3P_{11} unit cell (c) Cu_2P_7 2×2×2 supercell in which P–P connectivity is shown to highlight the P chains in the supercell structure. (d) Cu_3P_{11} 2×2×2 supercell with P–P connectivity shown to show P chains as in the Cu_2P_7 supercell.

Cu_3P_{11} and Cu_2P_7 which is not shared by CuP_2. Comparing the PXRD patterns of $C2/m$–Cu_2P_7 and Cm–Cu_3P_{11} show that Cm–Cu_3P_{11} is distinguished by a peak at a 2θ value of 16°, where $C2/m$–Cu_2P_7 has an indistinguishable peak at this point. Given the shared symmetry operations between Cm and $C2/m$ we expect to see peaks at the same 2θ values, but the intensities will vary between the structures. We deduce that these three phases could be verified using experimental PXRD, by using the peaks at $2\theta < 30°$ to distinguish between the phases.

$Cu_{3-x}P$ phases ($x \leq 1$)

Within the stoichiometry range $Cu_{3-x}P$ ($x \leq 1$), 4 unique Cu_3P phases, $Cu_{17}P_6$, Cu_8P_3, Cu_7P_3 and Cu_2P were found. Of these, $P6_3cm$–Cu_3P was the only phase previously experimentally determined, and had a formation energy 37 meV/atom above the convex hull tie-line. Olofsson identified the stoichiometry of $P6_3cm$–Cu_3P at 975 K to be between $Cu_{2.867}P$ and $Cu_{2.755}P$ due to Cu vacancies within the unit cell of $P6_3cm$–$Cu_{18}P_6$ (shown in Figure S1).[43] A study on low-temperature phases of $Cu_{3-x}P$ proposes phases from $Cu_{2.3}P$ to $Cu_{2.9}P$.[55] The lowest energy $Cu_{3-x}P$ ($x \leq 1$) phases identified in Table 1, $P1$–$Cu_{17}P_6$ ($Cu_{2.83}P$), $Cmc2_1$–Cu_8P_3 ($Cu_{2.66}P$), and $P1$–Cu_7P_3 ($Cu_{2.33}P$) are all defect structures of $P6_3cm$–Cu_3P with 1, 2, and 4 Cu vacancies respectively from the $P6_3cm$–$Cu_{18}P_6$ unit cell of Cu_3P. Of these three $P6_3cm$–Cu_3P defect structures, $Cmc2_1$–Cu_8P_3 ($Cu_{2.66}P$) has the smallest distance from the hull ($\Delta E = 26$ meV/atom). This corroborates previous DFT calculations suggesting Cu_3P has two Cu vacancies.[47]

In addition to the ICSD phase of $P6_3cm$–Cu_3P ($\Delta E = 37$ meV/atom), two other Cu_3P phases were found which are closer to the convex hull tie line than $P6_3cm$–Cu_3P; these are the $P2_1/m$–Cu_3P ($\Delta E = 30$ meV/atom) and $I\bar{4}3d$–Cu_3P phase ($\Delta E = 11$ meV/atom). The $P2_1/m$–Cu_3P phase is structurally related to the $Fm\bar{3}m$–Cu_2P ($\Delta E = 0$ meV/atom) phase (discussed in the following section). These two phases are shown in Figure 4, in which the $P2_1/m$–Cu_3P can be described as a stacking of the $Fm\bar{3}m$–Cu_2P phase. While the $Fm\bar{3}m$–

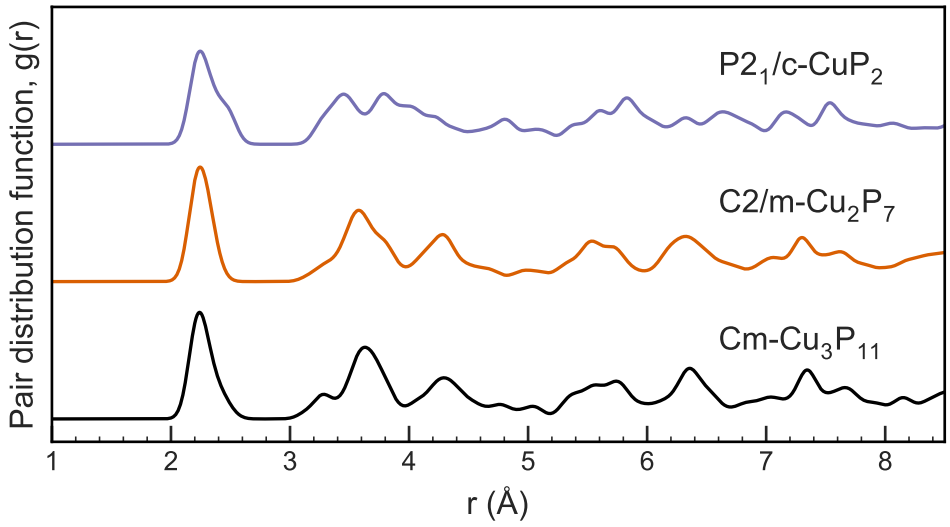

(a)

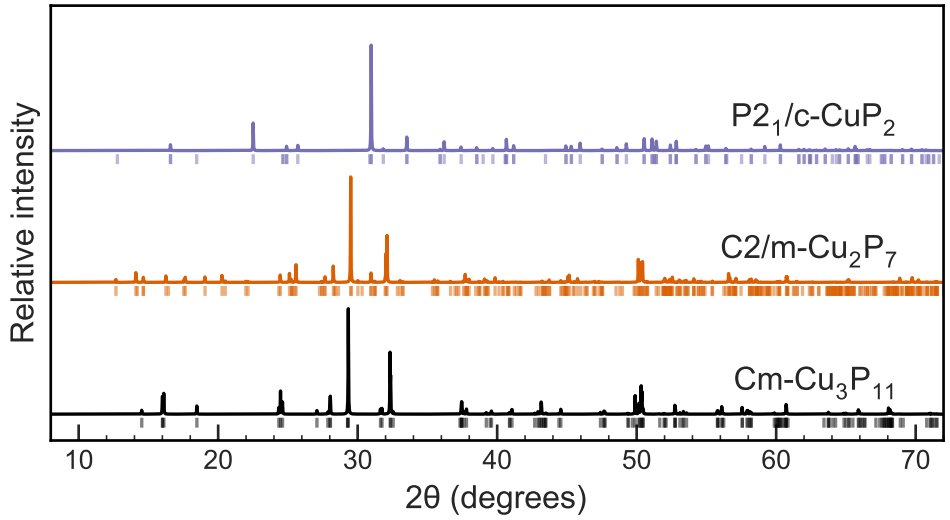

(b)

Figure 3: (a) Pair distribution function (PDF) of Cm–Cu_3P_{11}, $P2_1/c$–CuP_2 (ICSD 35282), and $C2/m$–Cu_2P_7 (ICSD 35281) shows all three have a first peak between 2.20 Å and 2.24 Å, while CuP_2 has two peaks around 3.6 Å, where both Cu_2P_7 and Cu_3P_{11} have one. All PDFs are artificially broadened with Gaussians of width 0.1 Å and PXRDs are calculated using a Cu K_α source. (b) The simulated PXRD patterns of both Cu_2P_7 and Cu_3P_{11} share peak positions, as is expected from their shared symmetries. The Cu_3P_{11} phase could be identified experimentally by the higher intensity peaks at $2\theta < 30°$, including a distinct peak at 16°, not present in Cu_2P_7. Details of PXRD calculations can be found in the Supporting Information .

Cu_2P phase has not been observed experimentally, it is likely that the two phases could be distinguished, given their distinct PDF and PXRD patterns shown in Figure S2. The PXRD pattern for $P2_1/m$–Cu_3P has additional low intensity peaks to the right of the 46° peaks, and is distinct from the other low-energy phases of Cu_3P as shown in Figure S2, which would further distinguish this phase in experiment.

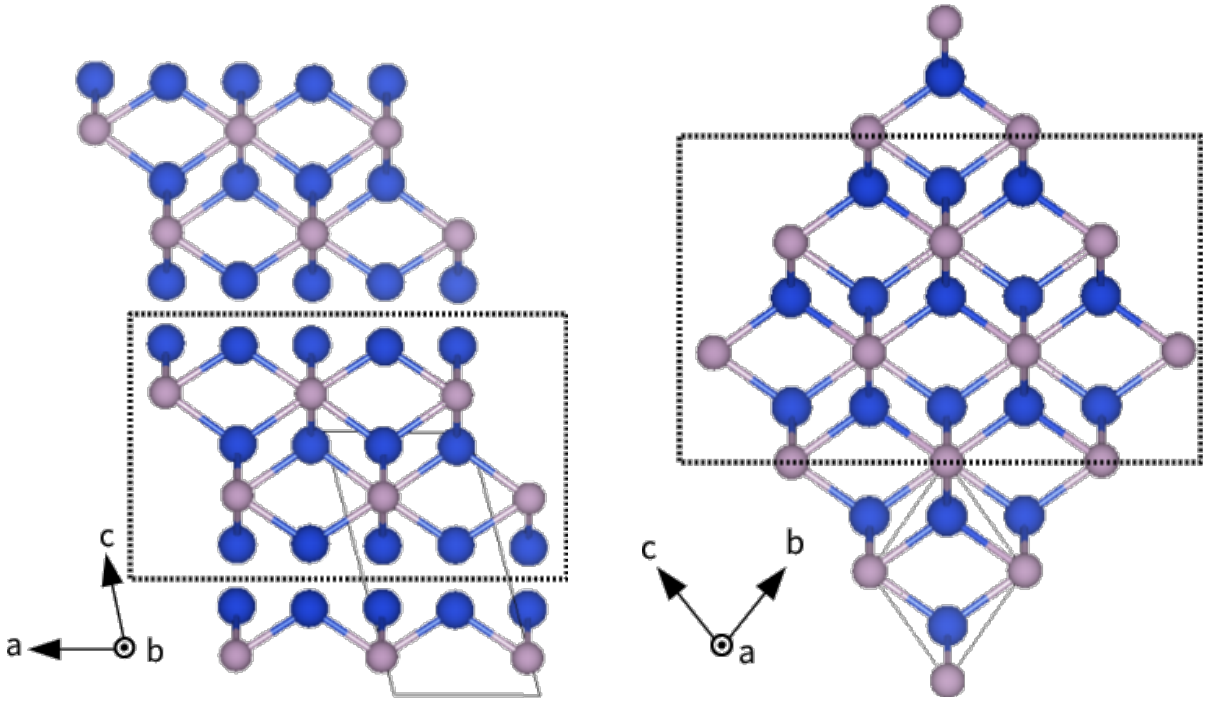

(a) $P2_1/m$–Cu_3P (b) $Fm\bar{3}m$–Cu_2P

Figure 4: $P2_1/m$–Cu_3P found by the GA and $Fm\bar{3}m$–Cu_2P from a swap with $Fm\bar{3}m$-Ir_2P. Here Cu atoms are colored blue and P atoms are colored pink. $P2_1/m$–Cu_3P structure can be described as a stacking of Cu_2P layers separated by Cu atoms. The stacking pattern which is present in both structures is indicated by the black dashed line surrounding the atoms in each structure. This is meant to guide the eye, and show the similarity in the two structures. The unit cells of each structure are outlined with a thin gray box. Cu_2P is predicted to be a stable 2D phase,[56] which could be layered to produce the Cu_3P phase shown in panel (a) here.

The lowest energy Cu_3P phase is an $I\bar{4}3d$ phase 11 meV/atom above the tie-line, which was identified by relaxing the prototype $I\bar{4}3d$–Cu_3As structure (ICSD 64715[49,57]). The $I\bar{4}3d$–Cu_3P structure is the highest symmetry Cu_3P phase, and is the only cubic phase in the set of low-energy Cu_3P structures. $I\bar{4}3d$–Cu_3P contains 8 formula units in the primitive unit cell,

and has 9-fold coordinated P atoms whereas $P6_3cm$–Cu_3P has 8-fold coordinated P atoms. The resulting crystal structures, shown in Figure S1, show two different long range orderings of the Cu sub-network. $P6_3cm$–Cu_3P has only one, 8-fold coordinated, P site which results in continuous zig-zag chains of Cu atoms surrounding the P, which are at the peaks of the buckles in the zig-zag. In $I\bar{4}$–Cu_3P, there are two 9-fold coordinated sites; one site at the center of the surrounding Cu (seen in Figure S1) and one at the edges, which together form a hexagonal Cu cage surrounding the P atom in the center. While both phases have high-coordinated P atoms, the $I\bar{4}3d$–Cu_3P shows a network of Cu atoms surrounding a central P atom, where $P6_3cm$–Cu_3P contains infinite Cu chains in the c direction.

Another trigonal phase, $P\bar{3}c1$–Cu_3P (ICSD 16841,[49] $\Delta E > 50\,\text{meV/atom}$) has the same structure as $P\bar{3}c1$–Cu_3As (ICSD 16840[49]), however it is 82 meV/atom above the convex hull tie-line. To the best of our knowledge, there are no reports of an $I\bar{4}3d$–Cu_3P phase, either experimentally or in a computational database. The PDF and PXRD patterns of $I\bar{4}3d$–Cu_3P given in Figure S2, show no relation to any other Cu_3P phase, or the $Fm\bar{3}m$–Cu_2P phase, thus, if energetically stable, it could be identified using PXRD in experiment.

$Fm\bar{3}m$–$\mathbf{Cu_2P}$

The $Fm\bar{3}m$–Cu_2P phase was found from the prototype $Fm\bar{3}m$-Ir_2P (ICSD 640898).[58] Comparing the Cu_2P phase to both Ir_2P and Rh_2P using PDFs in Figure S3 shows that the PDFs are identical between all three structures, and the PXRD plot of Cu_2P has the same peaks, all shifted to slightly higher values of 2θ due to structural relaxations in the geometry optimization of Cu_2P.

Previously, a 2D structure of Cu_2P was predicted theoretically as a buckled non-magnetic material,[56] in which the magnetism expected was inhibited by the buckled layers. The buckled layers from the 2D phase are also present in the bulk $Fm\bar{3}m$–Cu_2P, and the non-magnetic nature was confirmed in the bulk phase by the lack of spin-polarization in the density of states shown in Figure S4. The bulk $Fm\bar{3}m$–Cu_2P structure described above has

the same structural motifs as the 2D hexagonal phase found by Yang et al.,[56] and has the same electronic properties.

$Fm\bar{3}m$–Cu_2P lies on the convex hull tie-line, and is energetically more stable than both the experimentally confirmed phase of $P6_3cm$–Cu_3P, and its defect structure $Cmc2_1$–Cu_8P_3. Figure 5 shows the phonon dispersion for the $Fm\bar{3}m$–Cu_2P computed as mentioned in the Methods section. No imaginary phonon frequencies were present in the dynamical matrix (interpolated or otherwise), indicating that $Fm\bar{3}m$–Cu_2P is dynamically stable.

The electronic structure of $Fm\bar{3}m$–Cu_2P is related to the electronic structure of other $Fm\bar{3}m$ TMPs, suggesting it belongs to the same class of materials as $Fm\bar{3}m$-Ir_2P and Rh_2P. Of the TMPs in the Materials Project database,[59] 21 are insulating, and 68 are metallic with a high density of transition metal d-bands below the Fermi level. Figure 6 shows the electronic band structure and density of states of $Fm\bar{3}m$–Cu_2P projected by species along the high-symmetry path from SeeK-path used previously, and the density of states projected by angular momentum channel on a fine Monkhorst-Pack grid. The band structure shows that Cu_2P is a metal with P and Cu bands touching at the Γ point ~2.0 eV above the Fermi level. In addition there is a characteristic high density of flat bands localized on the Cu ions that exhibit d-character around 2.5 eV below the Fermi level. Calculating this band structure using the HSE06 functional (shown in Figure S5), a hybrid functional designed to correct for band gap underestimation, the gap at Γ between the Cu and P bands is closed.

Many M_2P phases (where M is a transition metal) have a structure similar to $P\bar{6}2m$-Ni_2P[60] and Fe_2P[61,62] in which the metal atoms sit in a cage of 3-fold coordinated P and 4-fold coordinated metal atoms. $Fm\bar{3}m$–Cu_2P is most similar to the other $Fm\bar{3}m$ TMPs, as it was derived from a the prototype structure $Fm\bar{3}m$-Ir_2P, and has 4-fold coordinated Cu with 8-fold coordinated P. The Cu_2P band structure in Figure 6 is also similar to those of Ir_2P and Rh_2P. In Rh_2P there is a directionally opened gap 1 eV above the Fermi level at the Γ point, not present in Cu_2P or Ir_2P (Cu_2P, Ir_2P and Rh_2P band structures calculated with spin-orbit coupling are given in Figure S6, the gapped region is outlined in black dashed

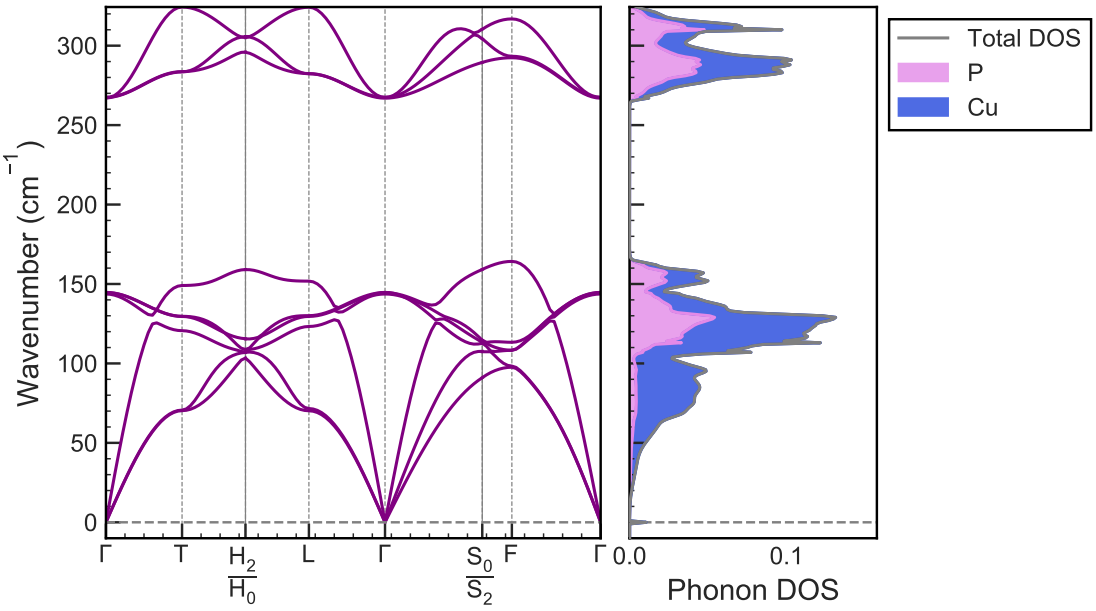

(a)

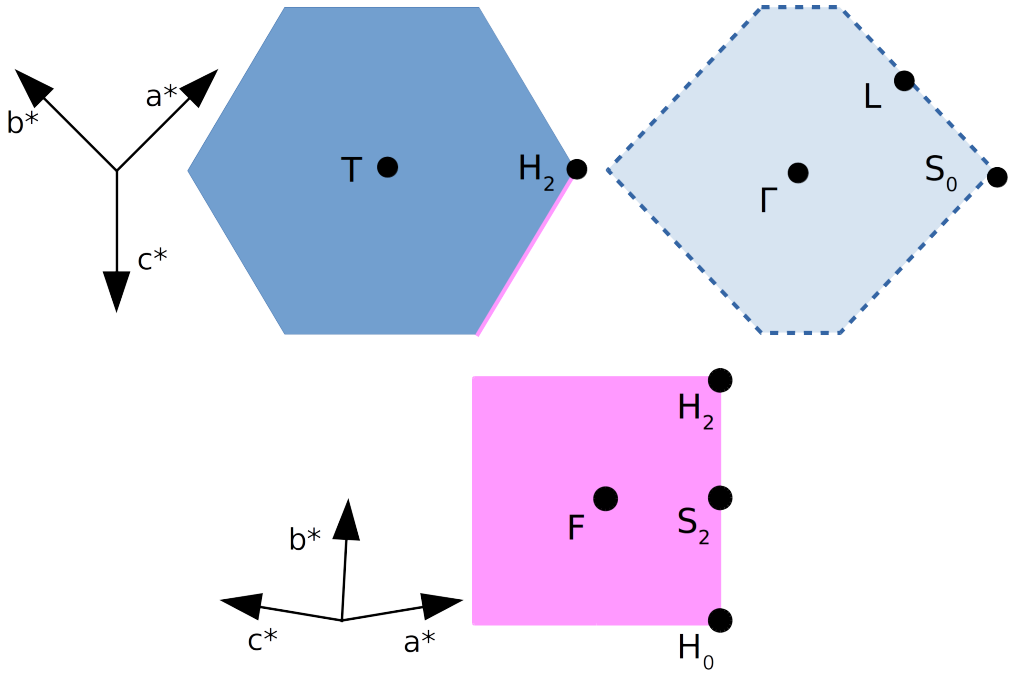

(b)

Figure 5: (a) Cu_2P phonon dispersion under the harmonic approximation and the corresponding Brillouin zone. Phonon dispersion and density of states were interpolated from the dynamical matrix calculated using the PBE *xc*-functional and the "C18" pseudopotential library, with a $2\pi\times0.03\,\text{Å}^{-1}$ k-point spacing, 500 eV plane wave cutoff, in a $2\times2\times2$ supercell using the finite displacement method (corresponding to a phonon q-point spacing of $2\pi\times0.046\,\text{Å}^{-1}$). (b) Brillouin zone is a truncated octahedron, with special points on each face labeled here. The dashed hexagon outline indicates the center of the Brillouin zone.

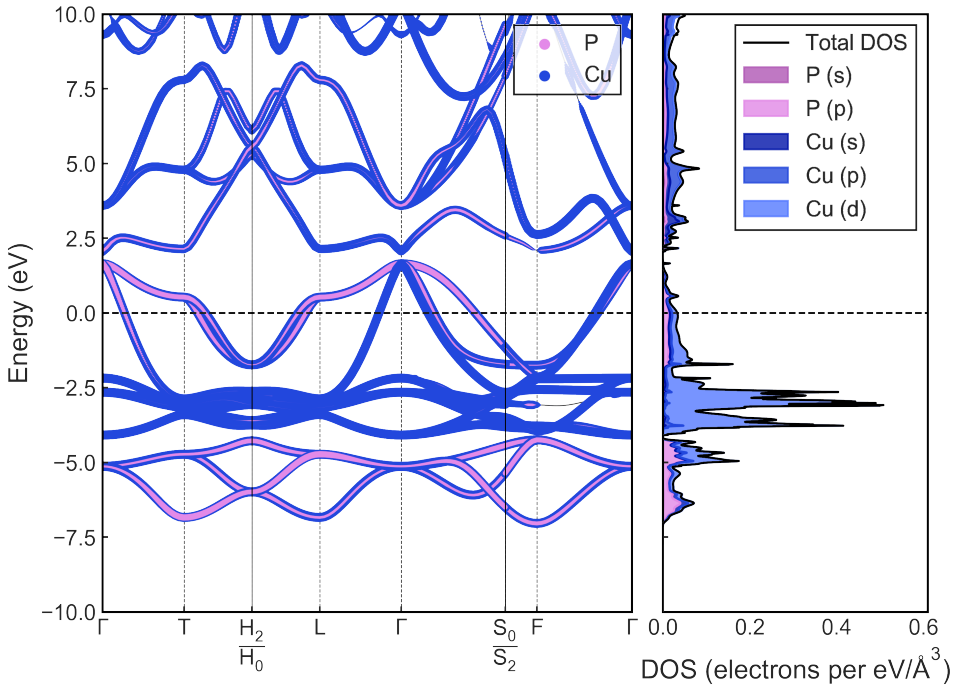

Figure 6: Electronic band structure of Cu_2P projected onto the Cu and P states and density of states projected onto the Cu s,p,d and P s and p states, for Cu_2P using an energy cutoff of 500 eV with $2\pi \times 0.03\,\text{Å}^{-1}$ k-point spacing and "C18" on-the-fly pseudopotentials. The projected band structure is produced by OptaDOS,[38] and band energies are calculated by CASTEP.[31]

line). Both of these structures exhibit spin-orbit coupling due to their heavy metal ions, while Cu has negligible spin-orbit coupling effects. The Rh_2P and Ir_2P band structures are calculated including spin-orbit coupling.

Finite-Temperature Phase Stability

The temperature-dependent convex hull was constructed by calculating the finite-temperature Gibbs free energies by including vibrational effects at the harmonic level[63] of several related structures on or near the convex hull from Figure 1. All structures within 20 meV/atom of the hull at 0 K were included in the finite-temperature hull; these were $Fm\bar{3}m$–Cu_2P, $I\bar{4}3d$–Cu_3P, $Cmc2_1$–Cu_8P_3 (the structure with 2 Cu vacancies from $P6_3cm$–Cu_3P discussed previously), CuP_2, CuP_{10}, Cu_2P_7, and Cu_3P_{11}.

The chemical potentials for this binary convex hull were *Cmca*-P (black phosphorus) and $Fm\bar{3}m$–Cu. Previously, Mayo *et al.* noted that the inclusion of semi-empirical dispersion corrections for black phosphorus changed the energetics of the convex hull,[26] and therefore it is not possible to combine optimized structures with and without dispersion corrections on the same convex hull. However, in order to obtain non-imaginary phonon frequencies of *Cmca*-P, it is necessary to account for dispersion. To account for this the many-body dispersion correction (MBD) was applied during the geometry optimization and phonon calculation.[40] Using PBE the distance between P chains in black phosphorus is 3.95 Å. By applying this correction, the P–P chain distance was reduced to 3.58 Å. In order to include the MBD black phosphorus on the convex hull in Figure 7a, we calculated the free energy of black phosphorus $F(T)$, at a given temperature T as,

$$F(T) = H + \Delta F^{MBD*}(T), \tag{3}$$

where H is the enthalpy without the dispersion correction, and $\Delta F^{MBD*}(T)$ is the free energy contribution at temperature T with the MBD dispersion correction, which includes the zero-

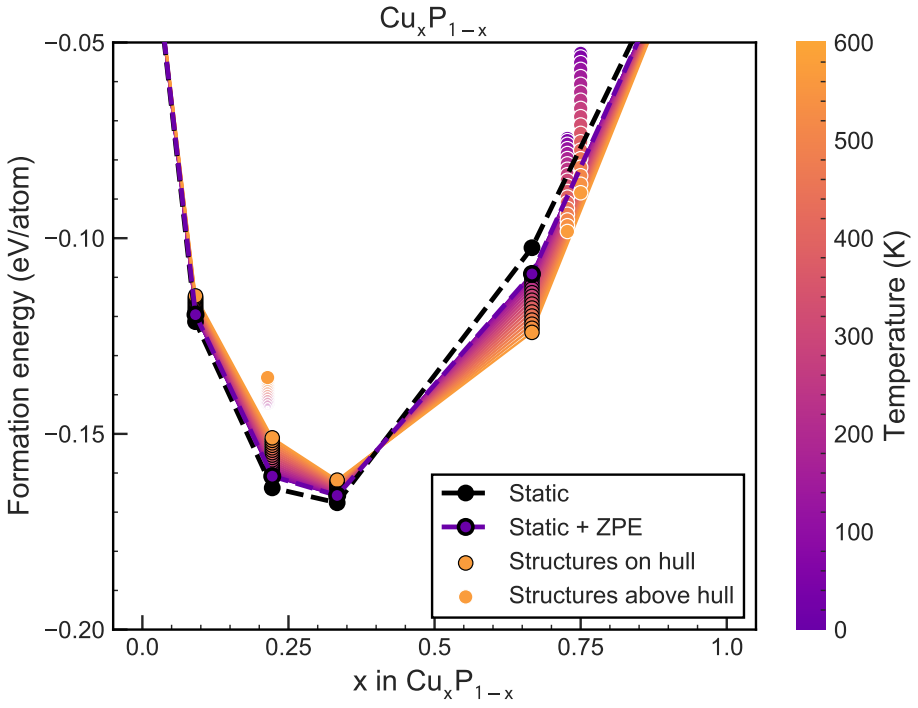

(a)

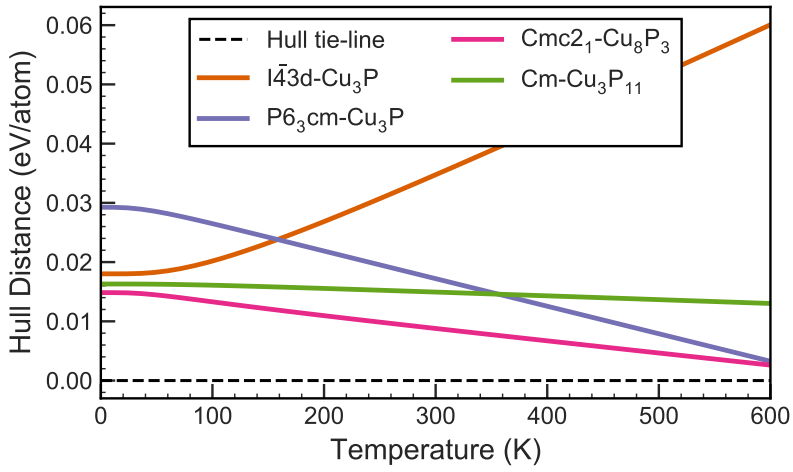

(b)

Figure 7: (a) Temperature-dependent convex hull with PBE xc-functional and MBD correction on the black phosphorus chemical potential. (b) Distance from the hull for the four structures which were above the convex hull tie-line at 0 K. All structures except $I\bar{4}3d$–Cu_3P get closer to the tie line as the temperature increases, suggesting they are stabilized by temperature. This agrees with the experimental evidence for Cu_8P_3 and $P6_3cm$–Cu_3P, and suggests that Cu_3P_{11} may form experimentally.

point energy. In this way the energies of black phosphorus were referenced to the ground-state energy without dispersion. The SCAN functional accurately describes the phonon modes of black phosphorus without any added dispersion corrections (i.e. no imaginary modes are observed) and therefore is used as a comparison to the MBD corrected PBE functional in Figure S7. Figure S7 shows that for any temperature T, both $\Delta F^{MBD}(T)$ and $\Delta F^{SCAN}(T)$ are on the same scale, only the zero-point energy is shifted (by 2.6 meV/atom) for the PBE+MBD calculation. Therefore, we expect the results of the PBE+MBD free energies to be comparable with non-dispersion corrected PBE free energies.

Using the MBD correction on black phosphorus in addition to the phonon modes of the previously mentioned phases of Cu–P, the hull in Figure 7a was constructed up to 600 K, above which no changes to stabilities are observed. A maximum value of 600 K was chosen so as not to approach the melting point of any phases, as the known phases of Cu–P typically have melt between 800 and 1200 K. Furthermore, the harmonic approximation is a limited approach, and at higher temperatures, anharmonicity should be accounted for. $Fm\bar{3}m$–Cu_2P remains on the hull at 600 K, suggesting it could be synthesized at high temperature. The convex hull is confirmation that the $Cmc2_1$–Cu_8P_3 phase formed from two Cu vacancies in $P6_3cm$–Cu_3P is the more stable phase at room temperature, as at 300 K, $Cmc2_1$–Cu_8P_3 is within 10 meV/atom of the convex hull as shown in Figure 7b. In addition, the destabilization of $I\bar{4}3d$–Cu_3P at high temperatures, shown in Figure 7b suggests that this phase is not experimentally realizable, and provides an explanation as to why it has not yet been experimentally synthesized. We can clearly see that $P6_3cm$–Cu_3P is stabilized at higher temperatures, as shown in Figure 7b, in which it is within 10 meV/atom of the convex hull at temperatures higher than 450 K.

Previous work on the $Cu_{3-x}P$ phases of $P6_3cm$–Cu_3P [47] confirms that the formation of two vacancies in Cu_3P is energetically stabilizing. By enumerating all of the possible structures with two Cu vacancies using the vacancy enumeration procedure described in the Methods Section, we have determined that the $Cmc2_1$–Cu_8P_3 phase with two Cu vacancies in the

6*c* Wyckoff positions is the lowest energy vacancy phase. Given the large number of ways to introduce these vacancies into the structure, configurational entropy will further stabilize this phase at high temperatures. To fully understand the nature of vacancy formation in $P6_3cm$–Cu_3P a full cluster expansion could be performed, which is beyond the scope of this paper.

Cu_2P as a Li-ion battery conversion anode

$Fm\bar{3}m$–Cu_2P was computationally predicted to be energetically stable as both a 2D material[56] and now in this article as a bulk phase. The previous sections predict the stability of $Fm\bar{3}m$–Cu_2P at temperatures up to 600 K, and characterize it as a metal with dispersive bands and delocalized conduction states at the Fermi level. An intuitive choice of application for Cu_2P lies in conversion anodes for Li-ion batteries, where previously both CuP_2 and Cu_3P were used as anodes with gravimetric capacities between 300 and 800 mAh/g.[11–14]

The crystal structure of $P6_3cm$–Cu_3P has a theoretical capacity of 363 mAh/g and experimentally has exhibited a range of capacities based upon the preparation method used.[13] The powdered Cu_3P anodes prepared by Bichat et al[13] ranged in initial capacity from 272 mAh/g using high-temperature synthesis in a silica tube to 527 mAh/g using low-temperature solvothermal synthesis respectively. In the solvothermal route, the Cu_3P powders were prepared with copper chloride, water, and NH_4OH with white phosphorus, which could have resulted copper oxide impurities leading to the initial capacity which is above the theoretical capacity of crystalline Cu_3P. Cu_3P powder synthesized by a solid-state reaction with red P in an ethanol suspension and Cu foil, the initial capacity of Cu_3P was 415 mAh/g.[14] Energy dispersive X-ray analysis showed that the stoichiometry was close to Cu_3P (though not exact) suggesting that this initial structure could have been within the stoichiometric range of $Cu_{3-x}P$ in order to achieve that initial capacity, in addition to the added capacity from likely oxide impurities.

In contrast, Cu_2P has a theoretical capacity of 509 mAh/g, which is above that of graphite

at 372 mAh/g. The metallic nature of Cu_2P further enhances its use as a Li-ion battery anode, enabling fast electronic transfer through the electrode of the battery. In fact, Cu is already widely used as a current collector in contemporary Li-ion batteries, and previous studies on Cu_3P nanorods suggest that Cu–P anodes create a synergistic chemical interface with the Cu-current collector which promotes cyclability.[15] Furthermore, because of its comparatively lower P content, volume changes during cycling are reduced, and therefore the degradation is likely to be less severe.[12]

The volume expansion for a conversion anode, with an overall conversion reaction

$$Cu_aP_b + 3b\,Li \longrightarrow a\,Cu + b\,Li_3P, \tag{4}$$

is calculated as,

$$\text{Volume expansion}\,(\%) = 100 \times \left(\frac{b\,V(\text{Li}_3\text{P}) + a\,V(\text{Cu})}{V(\text{Cu}_a\text{P}_b)} - 1 \right), \tag{5}$$

where $V(\text{Cu}_a\text{P}_b)$ is the volume per formula unit of each phase in the conversion reaction. Using this equation, the volume expansion of $Fm\bar{3}m$–Cu_2P is 99 %. This is comparable to the calculated volume expansion of $P63_cm$–Cu_3P, which is 86 %, and far superior to the volume expansion of CuP_2, which is 165 %. The volume expansion for each binary Cu–P phase is shown in Figure S8, confirming that Cu_2P has the lowest volume expansion of the four stable phases on the convex hull. Experimental reports on cycling of ball-milled CuP_2[12] suggest that volume expansion occurs, as after cycling for 10 cycles, the capacity is reduced by 50 %, although they give no estimate of the level of volume expansion in the cell. The expansion is partially mitigated through the use of nanostructuring,[11] which allows cycling for 200 cycles. However, there is still capacity fading in this case, which reiterates the need for a high capacity conversion anode with low volume expansion, so as to reduce the need for nanostructuring or other post-processing techniques to mitigate volume expansion. As both Cu_3P and Cu_2P have lower predicted volume expansions, and synthesized Cu_3P shows no

evidence of deleterious volume expansion,[13] it is likely that Cu_2P would also have minimal volume expansion in experiment.

Using the convex hull constructed in Figure 1 and the structures on the ternary hull of Cu–Li–P, a voltage profile was constructed from the DFT ground-state energies for both $Fm\bar{3}m$–Cu_2P and $P6_3cm$–Cu_3P. All of the known ternary structures were included in this hull: $P\bar{3}m1$–Cu_2LiP, $I4/mmm$–Cu_2LiP_2, $Immm$–$Cu_4Li_5P_6$ and $Cmcm$–$CuLi_2P$, as well as the binary Li–P structures $Cmcm$-Li_3P, $P2_1/c$-LiP, $P2_12_12_1$-Li_3P_7 and $I4_1/acd$-LiP_7. A plane wave kinetic energy cutoff of 700 eV was used, and all structures on the hull were re-relaxed at this higher cutoff. The ternary hull is shown in Figure S9, in which the pathways from Cu–P to Li are also shown, to depict how the voltage profiles for these Cu–P phases were calculated. The hull is shaded with a colormap to show the relative formation energy of phases on the hull, indicating that the Li–P phases have larger formation energies (and thus create a deeper convex hull) than the Cu–P phases.

Although Cu–Li phases are predicted to be stable under the approximation of PBE, the formation energy of the predicted Cu_3Li phase is only 26 meV/atom in the OQMD database[19,64] and no phases of Cu–Li are predicted at finite temperature in experiment.[65] Furthermore, Cu is used as a current collector in Li ion batteries specifically for its properties in resisting Li intercalation, and dead Li is found during cycling rather than Cu–Li phases.[66] Therefore, no Cu–Li compounds were included in the convex hull.

There are three ternary compounds on the Cu–Li–P hull in Figure S9; these are $I4/mmm$–Cu_2LiP_2, $Immm$–$Cu_4Li_5P_6$ and $Cmcm$–$CuLi_2P$. Experiments suggest that a hexagonal $LiCu_2P$ phase forms[67] during cycling, however the $P\bar{3}m1$–Cu_2LiP (ICSD 659706)[46] phase of this structure is 39 meV/atom above the hull at a plane wave cutoff of 700 eV.

From this ternary hull, shown in Figure S9, the voltage profile shown in Figure 8 was constructed. This hull is calculated as usual, without incorporating vibrational effects at 0 K. As the $P\bar{3}m1$–Cu_2LiP phase suggested in experiment[46,67] is 39 meV/atom above the convex hull, it cannot be in the voltage profile calculated in Figure 8. The 0 K voltage profile

includes the $I4/mmm$–Cu_2LiP_2 phase, which has been previously synthesized through a solid state reaction[68] and is a high T_c pnictide superconductor.[69] The $I4/mmm$–Cu_2LiP_2 phase has not, to our knowledge, been identified during cycling in Li-ion batteries previously.

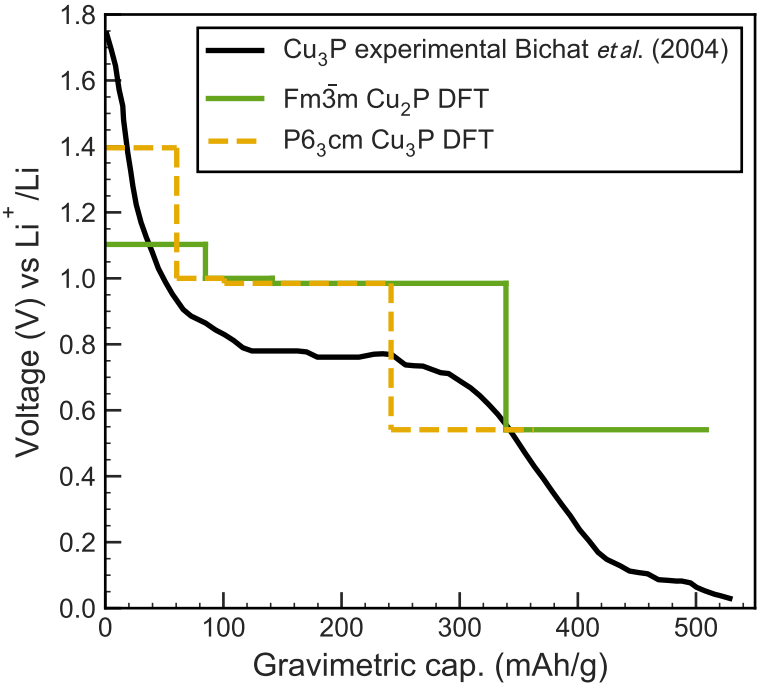

Figure 8: Ground-state voltage profile for $Fm\bar{3}m$–Cu_2P and $P6_3cm$–Cu_3P generated from the DFT ground-state structures of Cu–Li–P. The experimental profile was adapted from.[67] The experimental onset voltage matches closely with Cu_3P and shows a similar capacity to Cu_2P, though this added capacity is likely due to oxide impurities in the experiment.

Both Cu_2P and Cu_3P have the same overall reaction mechanism given by Equation 4, and the stable phases during the reaction from charging Cu_3P are given in Table 2. These reactions show Cu_2P operates in a narrower voltage window than Cu_3P and has a higher predicted gravimetric capacity. The predicted structures forming at each capacity and voltage are given in the 4^{th} column of Table 2. Though $Fm\bar{3}m$–Cu_2P undergoes the same lithiation process as $P6_3cm$–Cu_3P, $Fm\bar{3}m$–Cu_2P has a higher capacity of 508 mAh/g, and a higher average voltage of 0.86 V versus Li/Li^+, while $P6_3cm$–Cu_3P has a capacity of 363 mAh/g and average voltage of 0.91 V.

Each plateau in the ground-state voltage profile in Figure 8 represents a three phase region

of the ternary hull in which phases of Cu–Li–P are stable. Here, Cu_3P was 'stabilized' on the ternary hull by artificially excluding the CuP_2–Cu_2P_7 and Cu_2P phases. This is an approximation of a convex hull in which Cu_3P is on the tie-line which does not effect the formation energy (and thus predicted voltages) of the other phases. The experimental voltage curve shown in Figure 8 from[67] exhibits a similar trend in phase transitions along the cycle as the theoretical curve for Cu_3P.

Table 2: Reaction pathways for $Cu_nP + Li \rightarrow Li_3P + nCu$

Reaction Stage	Gravimetric Capacity (mAh/g)	Voltage (V)	Reaction Pathway
$Cu_2P + 3\ Li \rightarrow Li_3P + 2\ Cu$			
I	85	1.10	$\frac{1}{2}\ Cu_2LiP_2 + Cu$
II	141	1.00	$\frac{1}{6}\ Cu_4Li_5P_6 + \frac{4}{3}\ Cu$
III	338	0.98	$CuLi_2P + Cu$
IV	509	0.54	$Li_3P + 2\ Cu$
$Cu_3P + 3\ Li \rightarrow Li_3P + 3\ Cu$			
I	60	1.53	$\frac{1}{2}\ Cu_2LiP_2 + 2\ Cu$
II	101	1.00	$\frac{1}{6}\ Cu_4Li_5P_6 + \frac{7}{3}\ Cu$
III	242	0.98	$CuLi_2P + 2\ Cu$
IV	363	0.54	$Li_3P + 3\ Cu$

Conclusion

Using 4 different computational crystal structure searching techniques on the copper phosphides, several structures which lie close to the convex hull (within 20 meV/atom) were predicted, including Cm–Cu_3P_{11}, $I\bar{4}3d$–Cu_3P, and $Fm\bar{3}m$–Cu_2P; the experimentally characterized $P\bar{1}$–CuP_{10}, $C2/m$–Cu_2P_7 and $P2_1/c$–CuP_2 were all on the convex hull tie-line. By calculating the phonon dispersion curves of all structures within 20 meV/atom of the Cu–P convex hull, we constructed a temperature dependent convex hull which predicted $Fm\bar{3}m$–Cu_2P to be stable up to 600 K, while $I\bar{4}3d$–Cu_3P was destabilized with increasing temperature. We have also shown that the $Cmc2_1$–Cu_8P_3 phase formed from two Cu vacan-

cies at the 6c Wyckoff positions of $P6_3cm$–Cu_3P is stabilized with increasing temperature, and is within 10 meV/atom of the convex hull above 300 K. Experimental diffractometry on single-crystals of Cu_3P suggests that the phase has a range of stoichiometries between $Cu_{2.6}P$ and $Cu_{2.8}P$,[43,47] and Cu_8P_3 (or $Cu_{2.67}P$ equivalently) is within these bounds.

In addition to confirming the stability of $Cmc2_1$–Cu_8P_3, we also confirmed that Cm–Cu_3P_{11} remains metastable up to high temperatures as shown in the temperature dependent hull in Figure 7. While Cu_3P_{11} is unlikely to be used as a Li-ion battery anode, given its high P content, and therefore susceptibility to volume expansion, it could be a novel phase to consider within the Cu–P phase diagram. CuP_{10} was identified experimentally by preparing Cu_2P_7 in excess P;[70] given the structural similarity between Cm–Cu_3P_{11} and $C2/m$–Cu_2P_7 shown in Figure 2, it is possible that Cm–Cu_3P_{11} is also formed in excess P. Using the PXRD patterns presented in Figure 3, it may be possible to distinguish the Cm–Cu_3P_{11} phase from $C2/m$–Cu_2P_7 experimentally, from the change in peak intensity at 16°, and peak differences at 2θ values $< 20°$, however further experimental analysis is likely required given the low intensity of this peak.

Finally, $Fm\bar{3}m$–Cu_2P is the only phase identified through crystal structure prediction which was found on the hull at 0 K, and which remained on the convex hull at finite temperature, strongly suggesting it is possible to synthesize Cu_2P experimentally. Furthermore, its synthesis could provide a novel conversion anode, with favorable properties for Li-ion batteries. Hybrid functional calculations of the electronic properties of Cu_2P predict it to be isostructural and qualitatively similar electronically to both Rh_2P and Ir_2P, which are also $Fm\bar{3}m$ metals with dispersive bands at the Fermi level. This was confirmed using spin-polarized calculations, both with vector and scalar spin treatments, hybrid functional calculations using the HSE06 functional, and finally a projected band structure and density of states using PBE. This confirmation of the metallic nature of Cu_2P using a wide range of functionals and spin treatments suggests that this could be a better choice for anode than Li–P which are insulators with wide band gaps. Furthermore, the presence of such dispersive

bands, suggest high electron mobility within the anode, which would mitigate fast charge transfer between the Cu current collector and Li-ions. Finally, given its higher capacity (509 mAh/g) compared to Cu_3P, Cu_2P has potential as an experimentally realizable conversion anode which has a capacity that is competitive with graphite, conductive to promote electronic transfer within the anode, and less vulnerability to degradation compared to high P content conversion anodes due to reduced levels of cyclic volume changes.

Acknowledgments

The authors would like to thank Bartomeu Monserrat for his discussions on electronic structure, and Matthew Cliffe for his discussions on PXRD. We would also like to thank Can Koçer for looking over the manuscript text. AFH acknowledges the financial support of the Gates Cambridge Trust and the Winton Programme for the Physics of Sustainability, University of Cambridge, UK. MLE acknowledges the Engineering and Physical Sciences Research Council (EPSRC) Centre for Doctoral Training in Computational Methods for Materials Science, UK, for funding (EP/L015552/1). AJM acknowledges funding from EPSRC (EP/P003532/1). The authors acknowledge networking support via the EPSRC Collaborative Computational Projects, CCP9 (EP/M022595/1) and CCP-NC (EP/T026642/1). This work was performed using resources provided by the Cambridge Service for Data Driven Discovery (CSD3) operated by the University of Cambridge Research Computing Service (www.csd3.cam.ac.uk), provided by Dell EMC and Intel using Tier-2 funding from the Engineering and Physical Sciences Research Council (capital grant EP/P020259/1), and DiRAC funding from the Science and Technology Facilities Council (www.dirac.ac.uk).

Supporting Information Description

The Supporting Information document contains details of the simulation of powder X-ray diffraction patterns and pair distribution functions, as well as the electronic band structure

calculations using spin-orbit coupling. It contains all Supporting Information Figures referenced in the main text. All data is deposited at https://doi.org/10.17863/CAM.52272 in the Cambridge Repository. All analysis is on Github at `harpaf13/data.copper-phosphides` and Binder.

References

(1) Ramireddy, T.; Xing, T.; Rahman, M. M.; Chen, Y.; Dutercq, Q.; Gunzelmann, D.; Glushenkov, A. M. *Journal of Materials Chemistry A* **2015**, *3*, 5572–5584.

(2) Bhatt, M. D.; Lee, J. Y. *International Journal of Hydrogen Energy* **2019**, *44*, 10852 – 10905.

(3) Tarascon, J.-M.; Armand, M. *Nature* **2001**, *414*, 359–367.

(4) Kirklin, S.; Meredig, B.; Wolverton, C. *Advanced Energy Materials* **2013**, *3*, 252–262.

(5) Sun, M.; Liu, H.; Qu, J.; Li, J. *Advanced Energy Materials* **2016**, *6*, 1600087.

(6) Feng, L.; Xue, H. *Chem. Electro. Chem.* **2017**, *4*, 20–34.

(7) Lu, Y.; Yu, L.; Lou, X. W. D. *Chem* **2018**, *4*, 972 – 996.

(8) Boyanov, S.; Bernardi, J.; Gillot, F.; Dupont, L.; Womes, M.; Tarascon, J.-M.; Monconduit, L.; Doublet, M.-L. *Chemistry of Materials* **2006**, *18*, 3531–3538.

(9) Zhang, Y.; Zhang, H.; Feng, Y.; Liu, L.; Wang, Y. *ACS Applied Materials & Interfaces* **2015**, *7*, 26684–26690.

(10) Lu, Y.; Wang, X.; Mai, Y.; Xiang, J.; Zhang, H.; Li, L.; Gu, C.; Tu, J.; Mao, S. X. *The Journal of Physical Chemistry C* **2012**, *116*, 22217–22225.

(11) Kim, S.-O.; Manthiram, A. *ACS Applied Materials & Interfaces* **2017**, *9*, 16221–16227.

(12) Wang, K.; Yang, J.; Xie, J.; Wang, B.; Wen, Z. *Electrochemistry Communications* **2003**, *5*, 480 – 483.

(13) Bichat, M.-P.; Politova, T.; Pfeiffer, H.; Tancret, F.; Monconduit, L.; Pascal, J.-L.; Brousse, T.; Favier, F. *Journal of Power Sources* **2004**, *136*, 80 – 87.

(14) Pfeiffer, H.; Tancret, F.; Bichat, M.-P.; Monconduit, L.; Favier, F.; Brousse, T. *Electrochemistry Communications* **2004**, *6*, 263 – 267.

(15) Villevieille, C.; Robert, F.; Taberna, P. L.; Bazin, L.; Simon, P.; Monconduit, L. *Journal of Materials Chemistry* **2008**, *18*, 5956–5960.

(16) Ni, S.; Ma, J.; Lv, X.; Yang, X.; Zhang, L. *Journal of Materials Chemistry A* **2014**, *2*, 20506–20509.

(17) Chandrasekar, M.; Mitra, S. *Electrochimica Acta* **2013**, *92*, 47–54.

(18) Curtarolo, S.; Setyawan, W.; Hart, G. L.; Jahnatek, M.; Chepulskii, R. V.; Taylor, R. H.; Wang, S.; Xue, J.; Yang, K.; Levy, O.; Mehl, M. J.; Stokes, H. T.; Demchenko, D. O.; Morgan, D. *Computational Materials Science* **2012**, *58*, 218 – 226.

(19) Saal, J. E.; Kirklin, S.; Aykol, M.; Meredig, B.; Wolverton, C. *JOM* **2013**, *65*, 1501–1509.

(20) Hautier, G.; Fischer, C.; Ehrlacher, V.; Jain, A.; Ceder, G. *Inorganic Chemistry* **2011**, *50*, 656–663.

(21) Evans, M. *GitHub* **2016**, https://github.com/ml-evs/matador/releases/tag/0.9 (accessed May 11, 2020).

(22) Evans, M. *GitHub* **2017**, https://github.com/ml-evs/ilustrado/releases/tag/0.3b (accessed May 11, 2020).

(23) Harper, A. F.; Evans, M. L.; Darby, J. P.; Karasulu, B.; Koçer, C. P.; Nelson, J. R.; Morris, A. J. *Johnson Matthey Technology Review* **2019**, *64*, 103–118.

(24) others„ et al. *Journal of the American Chemical Society* **2014**, *136*, 16368–16377.

(25) Mayo, M.; Morris, A. J. *Chemistry of Materials* **2017**, *29*, 5787–5795.

(26) Mayo, M.; Griffith, K. J.; Pickard, C. J.; Morris, A. J. *Chemistry of Materials* **2016**, *28*, 2011–2021.

(27) Marbella, L. E.; Evans, M. L.; Groh, M. F.; Nelson, J.; Griffith, K. J.; Morris, A. J.; Grey, C. P. *Journal of the American Chemical Society* **2018**, *140*, 7994–8004.

(28) Hellenbrandt, M. *Crystallography Reviews* **2004**, *10*, 17–22.

(29) Pickard, C. J.; Needs, R. *Journal of Physics: Condensed Matter* **2011**, *23*, 053201.

(30) Deaven, D. M.; Ho, K. M. *Physical Review Letters* **1995**, *75*, 288–291.

(31) Clark, S. J.; Segall, M. D.; Pickard, C. J.; Hasnip, P. J.; Probert, M. I.; Refson, K.; Payne, M. C. *Zeitschrift für Kristallographie-Crystalline Materials* **2005**, *220*, 567–570.

(32) Perdew, J. P.; Burke, K.; Ernzerhof, M. *Physical Review Letters* **1996**, *77*, 3865.

(33) Vanderbilt, D. *Physical Review B* **1990**, *41*, 7892.

(34) Sun, L.-Q.; Li, M.-J.; Sun, K.; Yu, S.-H.; Wang, R.-S.; Xie, H.-M. *The Journal of Physical Chemistry C* **2012**, *116*, 14772–14779.

(35) Urban, A.; Seo, D.-H.; Ceder, G. *npj Computational Materials* **2016**, *2*, 1–13.

(36) Hinuma, Y.; Pizzi, G.; Kumagai, Y.; Oba, F.; Tanaka, I. *Computational Materials Science* **2017**, *128*, 140 – 184.

(37) Togo, A.; Tanaka, I. *arXiv* **2018**, http://arxiv.org/abs/1808.01590 (accessed Feb 19, 2020).

(38) Morris, A. J.; Nicholls, R. J.; Pickard, C. J.; Yates, J. R. *Computer Physics Communications* **2014**, *185*, 1477–1485.

(39) Nicholls, R. J.; Morris, A. J.; Pickard, C. J.; Yates, J. R. OptaDOS - a new tool for EELS calculations. Journal of Physics Conference Series. 2012; p 012062.

(40) Tkatchenko, A.; DiStasio Jr, R. A.; Car, R.; Scheffler, M. *Physical Review Letters* **2012**, *108*, 236402.

(41) Sun, W.; Dacek, S. T.; Ong, S. P.; Hautier, G.; Jain, A.; Richards, W. D.; Gamst, A. C.; Persson, K. A.; Ceder, G. *Science Advances* **2016**, *2*, e1600225.

(42) Zhang, G.-X.; Reilly, A. M.; Tkatchenko, A.; Scheffler, M. *New Journal of Physics* **2018**, *20*, 063020.

(43) Olofsson, O. *Acta Chemica Scandinavica* **1972**, *26*, 2777–2787.

(44) Lange, S.; Bawohl, M.; Weihrich, R.; Nilges, T. *Angewandte Chemie International Edition* **2008**, *47*, 5654–5657.

(45) Møuller, M.; Jeitschko, W. *Journal for Inorganic and General Chemistry* **1982**, *491*, 225–236.

(46) Schlenger, H.; Jacobs, H.; Juza, R. *Journal of Inorganic and General Chemistry* **1971**, *385*, 177–201.

(47) others„ et al. *Chemistry of Materials* **2015**, *27*, 1120–1128.

(48) Otte, H. M. *Journal of Applied Physics* **1961**, *32*, 1536–1546.

(49) Steenberg, B. *Arkiv Foer Kemi, Meralogi Och Geologi a Argka* **1938**, *12*.

(50) Owusu, M.; Jawad, H.; Lundström, T.; Rundqvist, S. *Physica Scripta* **1972**, *6*, 67–70.

(51) Zumbusch, M. *Journal for Inorganic and General Chemistry* **1940**, *243*, 322–329.

(52) Moeller, M. H.; Jeitschko, W. *Inorganic Chemistry* **1981**, *20*, 828–833.

(53) Crichton, W. A.; Mezouar, M.; Monaco, G.; Falconi, S. *Powder Diffraction* **2003**, *18*, 155–158.

(54) Thurn, H.; Krebs, H. *Acta Crystallographica Section B: Structural Crystallography and Crystal Chemistry* **1969**, *25*, 125–135.

(55) others,, et al. *Chemistry of Materials* **2018**, *30*, 7111–7123.

(56) Yang, L.-M.; Ganz, E. *Physical Chemistry Chemical Physics* **2016**, *18*, 17586–17591.

(57) Iglesias, J.; Nowacki, W. *Zeitschrift für Kristallographie-Crystalline Materials* **1977**, *145*, 334–345.

(58) Rundqvist, S. *Nature* **1960**, *185*, 31–32.

(59) Jain, A.; Ong, S. P.; Hautier, G.; Chen, W.; Richards, W. D.; Dacek, S.; Cholia, S.; Gunter, D.; Skinner, D.; Ceder, G.; Persson, K. A. *APL Materials* **2013**, *1*, 011002.

(60) Larsson, E. *Ark. Kemi* **1965**, *23*, 335–365.

(61) Carlsson, B.; Gölin, M.; Rundqvist, S. *Journal of Solid State Chemistry* **1973**, *8*, 57–67.

(62) Song, M.-S.; Kang, Y.-M.; Kim, Y.-I.; Park, K.-S.; Kwon, H.-S. *Inorganic Chemistry* **2009**, *48*, 8271–8275.

(63) Baroni, S.; de Gironcoli, S.; Dal Corso, A.; Giannozzi, P. *Rev. Mod. Phys.* **2001**, *73*, 515–562.

(64) Van de Walle, A.; Moser, Z.; Gasior, W. *Archives of Metallurgy* **2004**, *49*, 535–544.

(65) Okamoto, H. *Journal of Phase Equilibria and Diffusion* **2011**, *32*, 172–172.

(66) others,, et al. *Nature* **2019**, *572*, 511–515.

(67) Bichat, M. P.; Politova, T.; Pascal, J. L.; Favier, F.; Monconduit, L. *Journal of The Electrochemical Society* **2004**, *151*, A2074.

(68) Schlenger, H.; Jacobs, H. *Acta Crystallographica Section B: Structural Crystallography and Crystal Chemistry* **1972**, *28*, 327–327.

(69) Han, J.-T.; Zhou, J.-S.; Cheng, J.-G.; Goodenough, J. B. *Journal of the American Chemical Society* **2010**, *132*, 908–909.

(70) Bawohl, M.; Nilges, T. *Zeitschrift für Anorganische und Allgemeine Chemie* **2015**, *641*, 304–310.

For Table of Contents Only

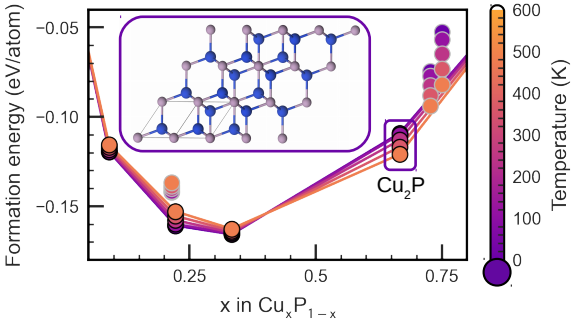

Supporting Information

Simulation of powder X-ray diffraction patterns and pair distribution functions

Powder X-ray diffraction (PXRD) patterns and pair distribution function (PDF) data were simulated using v0.9 of the `matador` package.[21] All PXRD patterns were calculated assuming a Cu-K_α source with wavelength 1.541 Å. PXRD peak intensities were corrected with atomic scattering factors, Lorentz-polarization correction and a thermal broadening term with an element-independent Debye-Waller factor ($B = 1$). All peaks were then artificially broadened with a Lorentzian envelope of width 0.03 °, which ignores instrument-dependent and momentum-dependent peak broadening. PDFs were computed from pairwise atomic distances in non-diagonal supercells to ensure all appropriate distances were considered within the region shown (1–8 Å). The pairwise distances were then collected as a histogram and broadened with a Gaussian envelope of width 0.01 Å. In these calculations, no element-dependence was introduced into the scattering behavior of each atom and thus intensities are not expected to match experimental data.

Details of band structure calculations

To calculate the spin-orbit coupled electronic band structures for Cu_2P, Ir_2P and Rh_2P, J-dependent pseudopotentials were used to account for coupling between orbitals, as implemented in CASTEP v20.1. All band structures were calculated using paths generated with SeeK-path,[36] with a k-point spacing of $2\pi \times 0.03$ Å^{-1}. The Cu J-dependent pseudopotential required a higher plane wave kinetic energy cutoff of 1000 eV, while both Rh and Ir required only 500 eV.

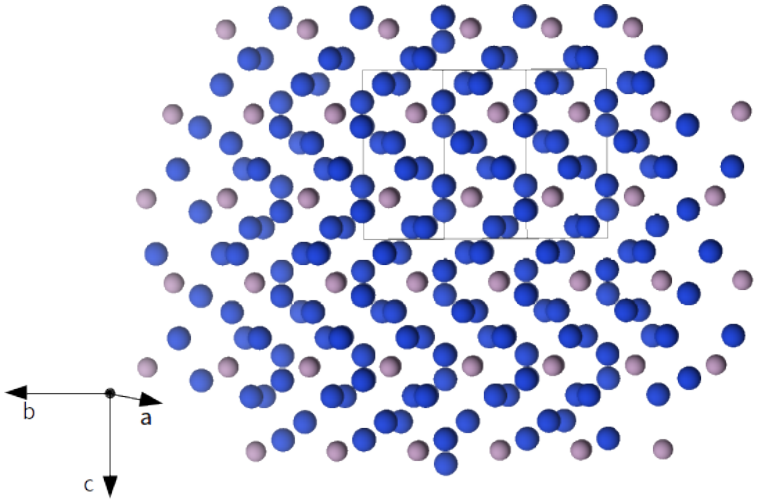

(a) $P6_3cm$–Cu_3P

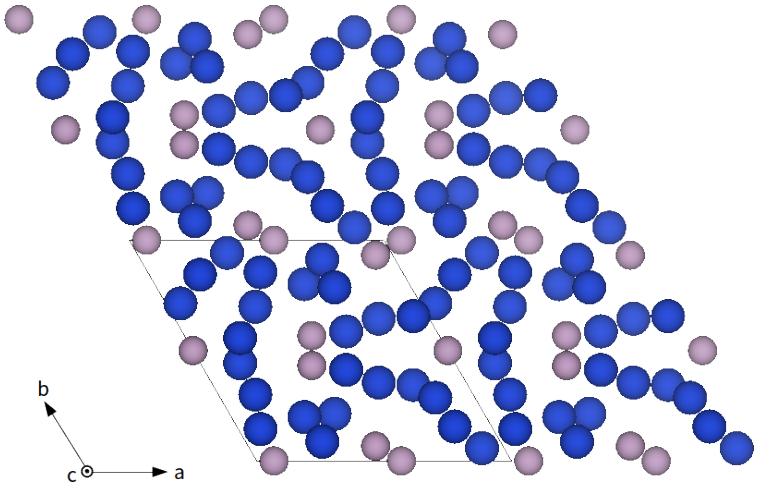

(b) $I\bar{4}3d$–Cu_3P

Figure S1: $P6_3cm$–Cu_3P (ICSD 15056) and $I\bar{4}3d$–Cu_3P from a swap with Cu_3As (ICSD 64715) shown as $2 \times 2 \times 2$ supercells without Cu–P connectivity to illustrate the symmetry of both structures.

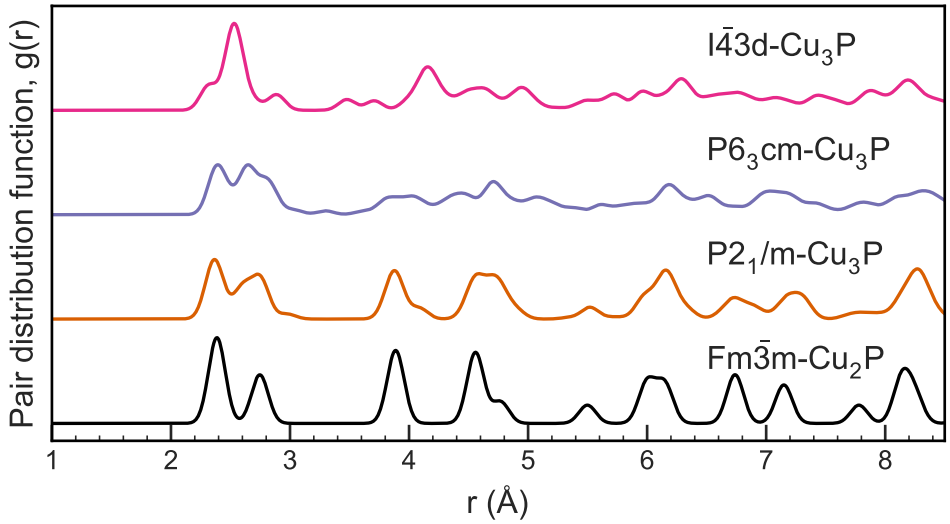

(a)

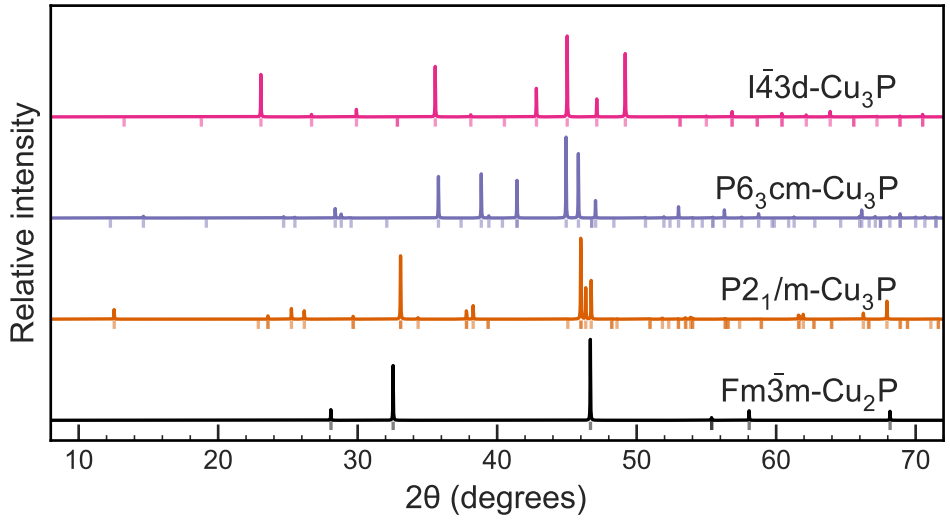

(b)

Figure S2: (a) PDFs of Cu_3P and Cu_2P all have two peaks between 2 and 3 Å except $I\bar{4}3d$–Cu_3P which has one sharp peak at ~2.6 Å. (b) PXRD patterns show peaks within 2° peaks in either $I\bar{4}3d$ or $P6_3cm$–Cu_3P. Details of the PDF and PXRD calculations can be found in the Supplementary Information.

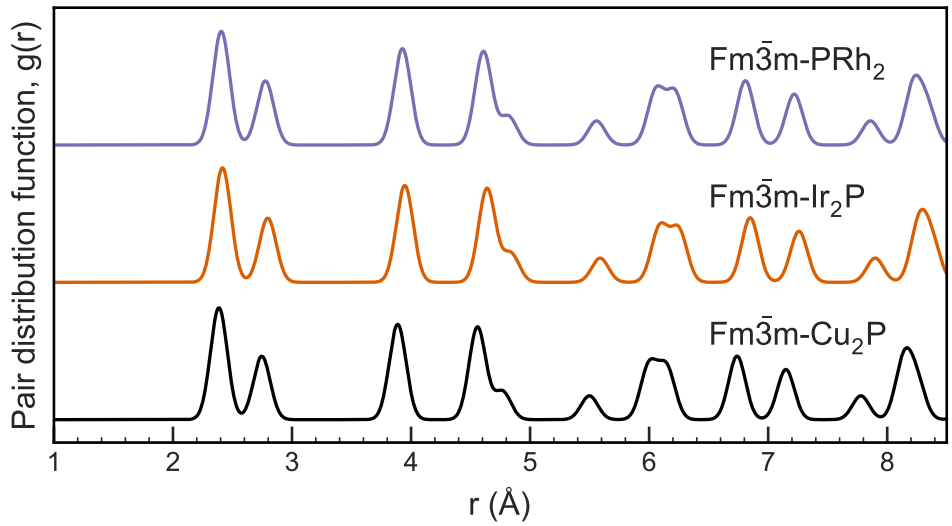

(a)

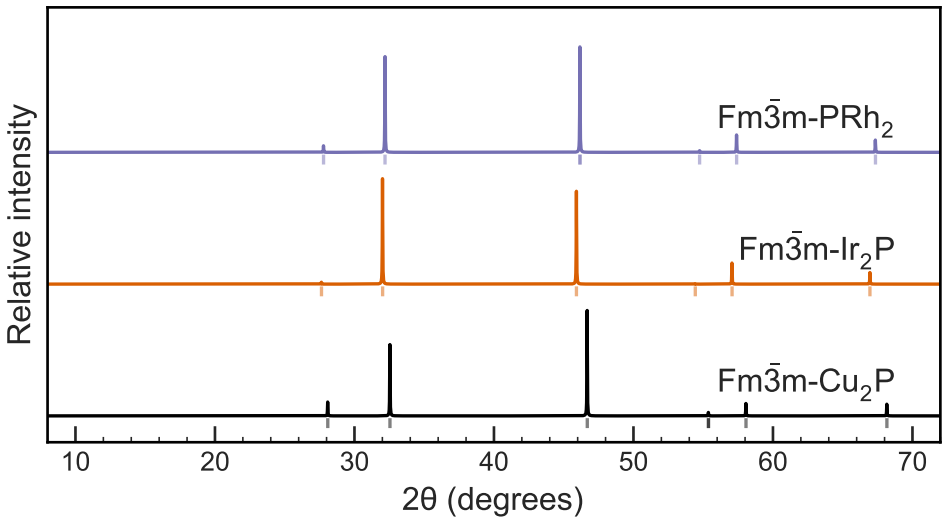

(b)

Figure S3: (a) PDF and (b) PXRD plots of Cu_2P, Ir_2P, and Rh_2P show all three structures are nearly identical. Cu_2P was identified from the prototype $Fm\bar{3}m$-Rh_2P and Ir_2P structures shown here. The Cu_2P peak shifts to higher 2θ values are a result of a cell-shrinking during geometry optimization to a side length of 3.89 Å, whereas Ir_2P and Rh_2P have cell side lengths of 3.95 Å *and* 3.93 Å *respectively. All PDFs are artificially broadened with Gaussians of width* 0.1 Å *and PXRD* source.

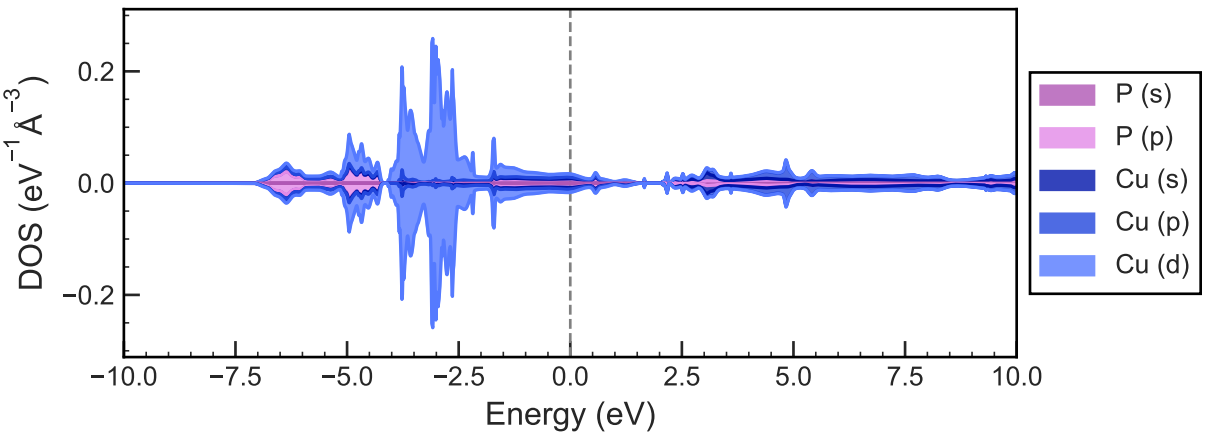

Figure S4: Cu_2P density of states calculated with PBE and plotted by spin channel, showing a non-magnetic state. The density of states are calculated by OptaDOS and projected onto the P s and p and Cu s, p, d states, as well as the up and down spins.

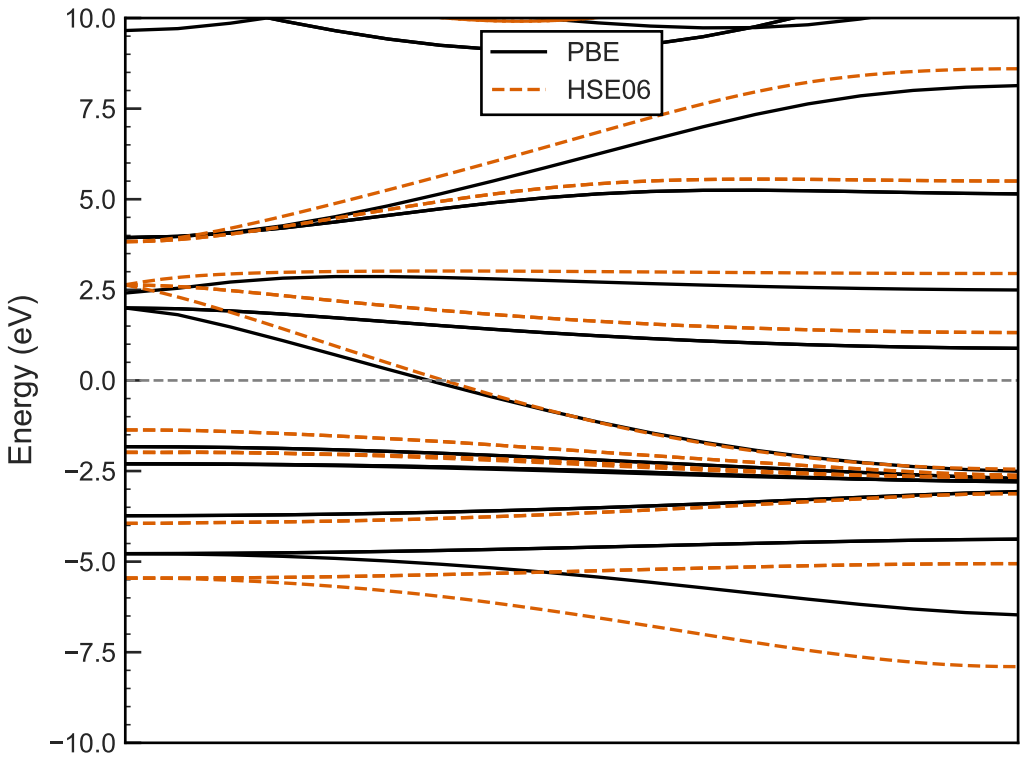

Figure S5: Comaparison between PBE and HSE06 band structures for Cu_2P calculated with CASTEP v18.[31] The HSE06 bands were offset by 0.35 eV and are shown with the dashed orange line, alongside the PBE bands in black, for the Γ to T path through the BZ. The bands are touching at 2.5 eV at the Γ point using the HSE06 functional where the PBE bands are non-degenerate at this point.

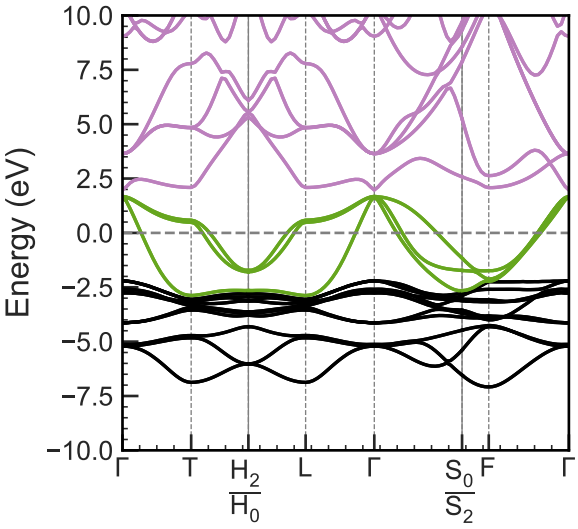

(a) Cu_2P

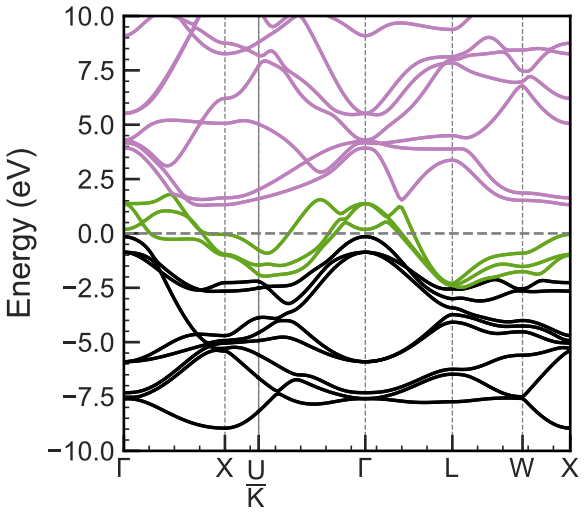

(b) Ir_2P

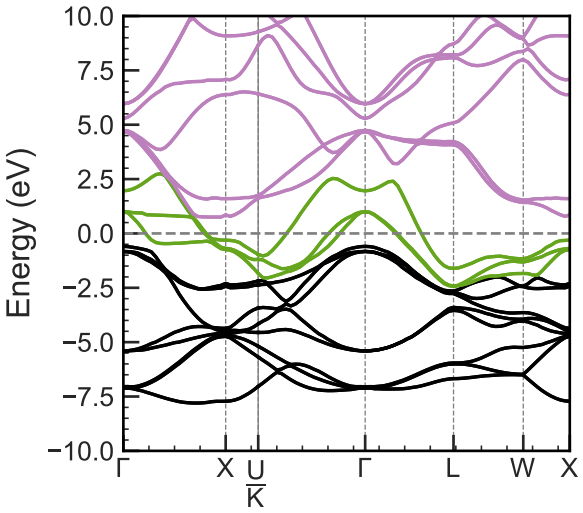

(c) Rh_2P

Figure S6: Cu_2P, Ir_2P and Rh_2P spin-orbit coupled electronic band structures calculated with CASTEP and OptaDOS.[31,38,39] All structures are metals with dispersive bands across the Fermi level (0.0 eV). The black dashed box in panels (b) and (c) shows the band gap crossing between two bands at the Γ point in Ir_2P and gap at the same location in Rh_2P.

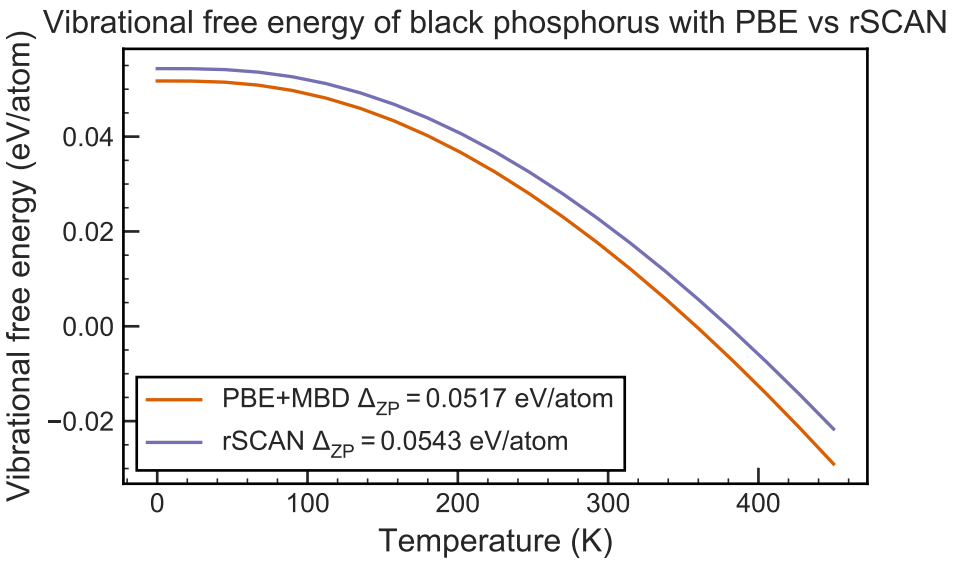

Figure S7: Comparison of free energies calculated using the rSCAN functional versus the PBE functional with MBD* correction which shows that the zero-point energy (Δ_{ZP}) is the only difference, justifying the use of PBE ground-state energies with MBD* correction for the chemical potential of black phosphorus as an equivalent method to using the rSCAN functional.

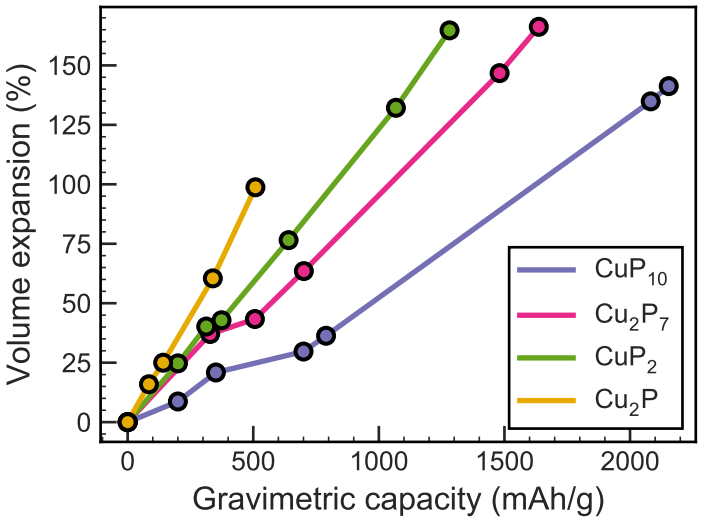

Figure S8: Volume expansion for 4 Cu–P phases. These lines follow the red pathways shown in Figure S9 where each point represents a two-phase region of the ternary hull, as a red pathway crosses over a black tie-line.

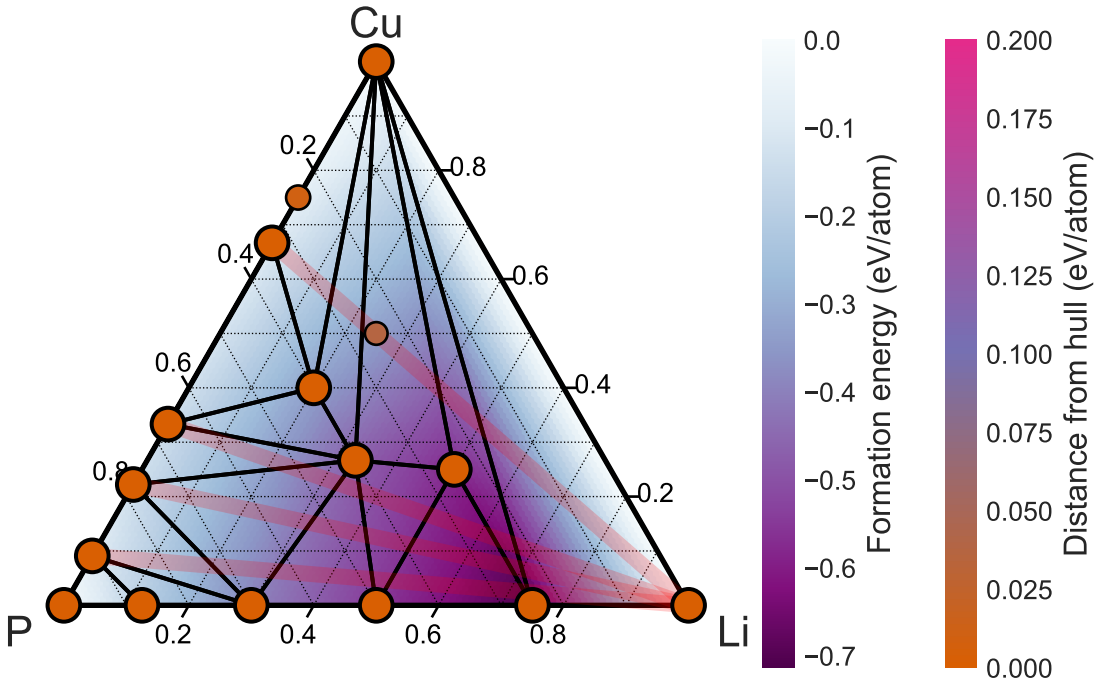

Figure S9: Ternary convex hull used in constructing the voltage profile for Cu_2P and Cu_3P. Structures on the hull are colored orange, and connected by tie-lines in black; red pathways show the ground-state conversion pathway from binary Cu–P structures to pure Li. Individual structures are represented by points which are colored by their distance from the hull. The ternary space itself is colored by the depth of the convex hull at that point. The red pathways are drawn from stable Cu–P phases towards Li; for example, this shows the phases which Cu_2P goes through during cycling before the final state of (Li_3P + 2 Cu).